Impact assessment of legacy wastes from ancient mining activities on current earthworm community

Anne-Lise Mariet, Honorine Gauthier-Manuel, Tiffany Lagiewski, Carole Bégeot, Anne-Véronique Walter-Simonnet, Frédéric Gimbert

To cite this version:

Anne-Lise Mariet, Honorine Gauthier-Manuel, Tiffany Lagiewski, Carole Bégeot, Anne-Véronique Walter-Simonnet, et al.. Impact assessment of legacy wastes from ancient mining activities on current earthworm community. Journal of Hazardous Materials, 2020, 393 (10), pp.122369. 10.1016/j.jhazmat.2020.122369 . hal-02930050

HAL Id: hal-02930050
https://hal.inrae.fr/hal-02930050v1

Submitted on 22 Aug 2022

Impact assessment of legacy wastes from ancient mining activities on current earthworm community

Anne-Lise Mariet, Honorine Gauthier-Manuel, Tiffany Lagiewski, Carole Bégeot, Anne-Véronique Walter-Simonnet, Frédéric Gimbert*

Department of Chrono-Environment, University of Bourgogne Franche-Comté, UMR UFC/CNRS 6249 USC INRA, 16 route de Gray, F-25030 Besançon Cedex, France

*Corresponding author:

Frédéric Gimbert

Tel.: +33 (0) 381 665 775

Fax: +33 (0) 381 665 797

E-mail address: frederic.gimbert@univ-fcomte.fr

Abstract

Mineral resource exploitation by human societies throughout history led to the deposit of mining and smelting wastes and the subsequent contamination of surrounding soils by trace metals. After several centuries, the impact of these legacy hazardous wastes may remain a cause of environmental concern, especially for indigenous soil invertebrate populations such as earthworms. Therefore, we conducted a passive biomonitoring campaign in a former metallurgical district (Vosges Mountains, eastern France). According to community descriptors, we evidenced a significant decrease of anecic and endogeic earthworm density in the former mining stations. To link these results to soil contamination and bioaccumulation levels in earthworm tissues, we propose an original modelling approach using nonlinear mixed-effects regression models. Beyond a dose-response relationship between metal internal concentrations and their levels in soils, we highlighted contrasted behaviors according to ecological groups (epianecics and endogeics most impacted). We interpreted these results in relation to some eco-physiological features without completely exclude the influence of textural characteristics of soil, especially for deep-burrowing species such as anecic strict. Nonetheless, the presence of earthworm populations currently living in highly contaminated sites and handling elevated internal concentrations raises the question of the acquisition of genetic adaptive traits and the trophic transfers of metals.

Keywords: trace metal; bioaccumulation; density; soil fauna; ecological group

1- Introduction

Throughout history, mining and smelting activities of metals such as iron (Fe), copper (Cu), lead (Pb), or silver (Ag) have played a leading role in the socio-economic development of human societies (Tylecote, 1987). However, at the same time, they generated significant amounts of potentially contaminated wastes whose weathering led to the release of trace metals (TMs) in the environment. In Europe, the former mining district of Sainte-Marie-aux-Mines (Vosges Mountains, eastern France) is known for its metal exploitation over the last millennium and especially Pb and Ag during the 15th-16th centuries (Fluck, 2006). In this particular district, it is estimated that more than 10% of the area is nowadays covered by several types of metallurgical wastes, i.e., ore dumps, slags, and ore-washing sediments (Fluck, 2000; Mariet et al., 2014). Persisting just a few centimeters deep, they affect both the physical (structure, texture) and chemical properties of current soils. For instance, the contamination by TMs is very elevated (up to several tens of thousands of mg_{Pb} kg^{-1} soil) and still highly available for potential transfers (Mariet et al., 2017b). Hence, using an active biomonitoring approach with the land snail *Cantareus aspersus*, it has been recently demonstrated that TMs from medieval mining activities (Pb-Ag extraction) were still bioavailable for this soil invertebrate (Mariet et al., 2016) and represent a risk for environmental health (Mariet et al., 2017a). But what about the current impacts of this legacy contaminated wastes on invertebrate populations living locally on these sites? To answer this question, we conducted a passive bioindication campaign in the former mining district of Sainte-Marie-aux-Mines by sampling earthworms at forested stations subjected to different mining operations and presenting a contamination gradient.

As key organisms of soil functioning, earthworms are well recognized as good indicators of environmental quality since they respond to a variety of environmental and ecological factors such as changes in soil use and contamination (Pérès et al., 2011; Tondoh et al., 2007). Moreover, although abundance is a classical endpoint for the assessment of earthworm community responses to environmental stress, ecological structure (i.e., the proportion of three main morpho-ecological groups: epigeic, endogeic and anecic) seems to be a more sensitive indicator of soil pollution. Indeed, Pérès et al. (2011) showed that soil contamination by PAHs and metals in industrial wastelands did not lead to a modification of earthworm abundance although the ecological structure was strongly impacted. In the same line, Nahmani et al. (2003) found, in soils from a former zinc smelter complex, a global reduction of earthworm densities in relation with an eradication of endogeic species and a reduction of epigeics.

The objectives of this study were, therefore, to assess the responses of the current earthworm community to past mining activities dating from several centuries ago and for which only scarce data are available in the literature. The impact on the community will be assessed by various community descriptors, as the density and ecological group distribution of earthworms, and originally completed by statistical consideration of bioaccumulation levels of several TMs in earthworm tissues belonging to different morpho-ecological categories.

2- Material and methods

2-1- Study sites

The study site is located in the former mining district of Sainte-Marie-aux-Mines (Vosges Mountains, France). Four forested stations (100 m²), called MA5, CF20, CF28, and CF29, were chosen according to their soil TM concentrations (Table 1) and to the presence of various types of mining wastes: ore dump on CF28, ore-washing sediments on CF29, and tailings from ancient mining wells on CF20. Lastly, according to the low TM concentrations measured in soils, station MA5 constitutes the control station. The habitat descriptors, in terms of dominating tree species and main physicochemical characteristics, are presented in Table 2. More details are also available in Mariet et al. (2016).

2-2- Sampling procedures and earthworm determination

For each station, sampling of autochthonous earthworms was carried out in spring (April) following the mustard method (Singh et al., 2016). Two spreadings (10 L each) of freshly diluted mustard (15 g L^{-1}) were applied, with an interval of 15 minutes, on a triplicate surface of 1 m^2 representative of the entire station. Then, the earthworm sampling was completed by hand sorting up to 30 cm depth (Pelosi et al., 2009). Sampled animals were rinsed and sorted by ecological groups (Bouché, 1977): epigeics, endogeics, epianecics, and anecic strict. The earthworms were left to empty their guts for 48 hours in moistened Petri dishes, individually weighted, pooled by ecological groups, and sacrificed at -80°C. For each station and ecological group, some individuals were stored in 95% alcohol for identification at the species level, when possible, using Bouché's key (1972).

Soils were also sampled at each sampling plot at three depths of the soil profile: 0-5 cm, 5-15 cm, and 15-30 cm. They were sieved to 2 mm, dried at 30°C, and stored for further TM analyses. According to their ecological niche, ecological groups were associated with particular soil depths: 0-5 cm for epigeic earthworms, 15-30 cm for endogeic earthworms, and 0-30 cm for anecic earthworms.

2-3- Trace metal analyses

The total concentrations of Ag, arsenic (As), cadmium (Cd), cobalt (Co), and Pb in soils (Table 1) were measured on dried samples after hot *aqua regia* digestion (HNO_3:HCl, 2:5, v/v) by ICP-MS (Thermo X2 Series) at the Chrono-Environment Laboratory. These five metals were chosen according to their significant contents in exploited ores and identified as anomalous elements in soils (Mariet et al., 2016). The analytical precision and accuracy were checked using a standard reference material (SRM) (Sigma Aldrich CRM052 Loamy Clay 1) with recovery rates of 97 ± 4 %, on average for all TMs.

Earthworms were freeze-dried, ground, and digested in HNO_3 by hot mineralization before ICP-MS analyses (Thermo X2 Series). Analytical precision and accuracy were checked using SRM (TORT-2, Lobster hepatopancreas; National Standard, Ottawa, ON, Canada). The recovery rates were 100 ± 13%, on average, for all TMs.

2-4- Soil physicochemical characteristics

Organic matter (OM) content, pH_{water} and texture (sand, silt, and clay) were determined on soils (0-30 cm) by the Laboratoire d'Analyse des Sols at the Institut National de la Recherche Agronomique (INRA) in Arras (France), which has earned COFRAC (French Accreditation Committee) accreditation n°1-1380 for its analytical quality of soil characteristics (Table 2).

2-5- Statistical analyses

The TM concentrations in soils were compared among both the stations and depths using a Kruskal-Wallis test ($p<0.05$) followed by a post-hoc multiple comparison (pgirmess R package). Difference of distribution of ecological groups between stations has been tested by Chi-square test ($p<0.05$). Then, differences of total density or density of ecological groups between stations were tested using Tukey HSD ($p<0.05$). The same procedure was used to highlight significant differences of biomass (Figure S1).

Principal component analysis (PCA) was carried out to assess the co-variation between community descriptors (total density and biomass), soil contamination (total Ag, As, Cd, Co, and Pb concentrations) and soil characteristics as texture (sand and silt contents), pH, and OM content.

The relationships between TM concentration in earthworms and soil contamination on the one hand and, on the other hand, earthworm density and TM concentration in earthworms were tested separately using nonlinear mixed-effects regression models (nlme R package), integrating the earthworm ecological group as fixed effect and the sampling plot as random intercept. The following models were used:

$$[TMs]_{earthworm} = a * \ln([TMs]_{soil}) + b$$

$$density = d0 * \exp(-k * [TMs]_{earthworm})$$

For all of the models, when residuals were skewed, variance functions (power and exponential) were applied, and the best model was selected according to Akaike's Information Criterion (pgirmess R package). The effect of ecological group was tested using a likelihood-ratio test (LRT, $p<0.05$). When a significant relationship was found, pairwise Wald t-tests of the estimated coefficients were carried out between ecological groups by re-ordering treatments in nlme models using the *relevel* R function (stats R package).

All of the statistics were performed with R (3.4.0) (R Core Team, 2014).

3- Results

3-1- Earthworm community description

The main representative species of each ecological group are summarized in Table 3. The earthworm communities were quite similar between the stations studied with *Lumbricus* sp. in the epigeic group, *Aporrectodea caliginosa* in the endogeic group, *Lumbricus rubellus* in the epianecic group and *Aporrectodea* sp. in the anecic strict group. An endemic species of the Vosges Mountains, *Allolobophora zicsii* (Bouché, 1972), an endogeic, was sampled in the MA5 station (Table 3).

The total density of earthworms sampled at each station showed significant differences with average values of 57 ± 26, 41 ± 10, 9 ± 4 and 10 ± 2 ind m^{-2} for MA5, CF20, CF29, and CF28, respectively (Fig. 1). The density of epigeic earthworms was not significantly different between each station, comprised between 4 and 6 ind m^{-2}. For the other ecological categories, the stations can be grouped into two lots based on significant differences of density: on the one hand, MA5 and CF20, and on the other hand, CF29 and CF28 with lower densities of epianecics, anecic strict, and endogeics (Fig. 1). The same pattern was observed for the biomass of earthworms (Figure S1). The highest average density was reached by the anecic strict in MA5 (45 g m^{-2}) and CF20 (25 g m^{-2}), although their density was the lowest in the stations CF29 (0.2 g m^{-2}) and CF28 (0 g m^{-2}).

The multivariate analysis allowed linking the community descriptors with the physicochemical characteristics of the stations (Fig. 2). The first axis of the PCA (65% variance explained) exhibited a gradient contrasting the stations according to their contamination by TMs (MA5 and CF20 vs. CF29 and CF28). The density and the biomass of earthworms were negatively correlated to the concentrations of TMs in soils. The second and third axis of the PCA (16% and 13% variance explained, respectively) separated stations according to the soil texture (axis 2) and pH/OM content (axis 3). Among soil characteristics, the texture is correlated, negatively for sand content and positively for clay content, to the density and biomass of earthworms.

3-2- Bioaccumulation of TMs by earthworms

The regressions between TM concentrations in whole earthworm tissues and their levels in soils showed significant dose-response relationships for Ag, As, Co, and Pb, but not for Cd ($p = 0.755$) (Fig. 3A and Table S1). The consideration of the earthworm ecological group did not improve the regression for Cd but allowed to distinguish different responses for the other

TMs considered (Fig. 3B). Hence, for Co, only endogeic earthworms showed internal concentrations significantly increasing with soil contamination (p = 0.014, Table S1). For Ag, a significant and similar relationship between bioaccumulation and soil concentration was highlighted for the epigeics, the endogeics and the epianecics (Fig. 3B and Table S1), while no significance was found for the anecic strict, with average internal concentrations of 0.91 ± 0.26 $\mu g\ g^{-1}$. The bioaccumulation of As and Pb by earthworms was important (reaching 103.88 $\mu g_{As}\ g^{-1}$ and 10,368.06 $\mu g_{Pb}\ g^{-1}$ on CF28) and was significantly related to soil concentration for all ecological groups (Fig. 3B). More precisely, for these two TMs, the epianecics showed the most marked responses, followed by the endogeics, the epigeics, and finally the anecic strict (Table S1).

3-3- Earthworm density response to TM bioaccumulation

Taking into account all the data, significant and negative relationships were found between earthworm density and their internal concentrations of Ag, As, and Pb. It was not the case for Cd (p = 0.533) and Co (p = 0.133) (Fig. 4 and Table 4). However, considering each ecological group, various response patterns are highlighted. Thus, it appears that the density of epianecics was negatively affected by the soil contamination for the five TMs considered (Table 4). Except for Cd (p = 0.880), similar results were reported for endogeic earthworms. Conversely, no significant influence of TM accumulation on the density was observed for the epigeic earthworms for all TMs. Finally, only internal concentrations of As and Pb were significantly associated with a decline in the anecic strict density (Table 4).

4- Discussion

4-1- Bioavailability of legacy contamination

The studied sites were characterized by the presence of various mining wastes deposited several centuries ago, which constitute a chronic and diffuse source of TM release to the surrounding soils (Mariet et al., 2014). Physico-chemical analyses also revealed that the type of mining waste drives the contamination levels in soils and the availability of TMs (Ettler, 2016; Mariet et al., 2017b). Hence, the sampled earthworms at the four stations showed marked differences in their internal concentrations of numerous TMs, which testifies to their current bioavailability to earthworms as previously demonstrated for other soil-dwelling invertebrates, i.e., snails (Mariet et al., 2016). Interestingly, earthworms (this study) and snails (Mariet et al., 2016) led to similar observations although these two bioindicators were used in different approaches, i.e., passive and active biomonitoring, respectively. The concentrations of TMs in the earthworm tissues of the control station (MA5) were of the same order as those reported from the literature for non-contaminated forest sites (Ma, 2004; Morgan and Morgan, 1990; Spurgeon and Hopkin, 1996). Lead, Ag, As, and Co bioaccumulation in earthworms respond to their concentrations in the soils while Cd does not. This could be explained by the relatively low concentration of this element in soils and its high leachability, especially under acidic conditions (Rékási and Filep, 2015). The largest TM tissue concentrations were observed for Pb (>10,000 mg kg^{-1} dry weight at CF28) and were comparable to those measured in heavily contaminated sites (Ernst et al., 2008; Ma, 2004). A study recently showed that despite the age of the mining deposits, ageing attenuation was low for Pb, which was still under bioavailable forms (Mariet et al., 2017b). Arsenic reached more than 100 mg kg^{-1} dry weight in earthworms collected at ore dump station CF28, but these values are lower than those found in the literature, even for mining sites (see for instance, Button et al., 2012), probably in relation to the influence of acidic soil pH on As speciation, mobility, and transfer (Wilson et al., 2010). For Ag and Co, the lack of published data concerning their accumulation in earthworms makes the comparisons with our results difficult. However, the significant concentrations measured in earthworms dwelling in mine waste deposit stations (in average 1.3 mg_{Ag} kg^{-1} in CF28 and 5.3 mg_{Co} kg^{-1} in CF29) compared to the control station (MA5) indicate a relatively high exposure to these elements exploited in the valley until the 18th century (Fluck, 2000).

Bioaccumulation abilities also depend on the earthworm ecological category. Indeed, in our study, endogeic, and epianecic earthworms showed the highest internal concentrations followed by epigeics and anecic strict. This could be explained by several eco-physiological factors. First, species differences in tissue metal concentration may largely reflect differences in niche separation (Morgan and Morgan, 1999; Qiu et al., 2014). The vertical distribution of different species in the soil profile determines to some extent the exposure of earthworms to contrasted TM bioavailable pools. For instance, epigeic earthworms are less exposed than geophagous species due to their saprophagous feeding behavior on the surface organic horizons of soils and their limited exposure route through dermal surface (Langdon et al., 2003). The results concerning earthworms belonging to the anecic strict category confirm the general tendency toward lower metal contents in tissues of deep-burrowing species (Ernst et al., 2008; Suthar et al., 2008; Tischer, 2009). However, this result was not really expected in our particular context of ancient mining contamination characterized by an increasing contamination with depth. The anecic strict are therefore exposed to elevated total TM concentrations but only low available fractions due to the sequestration of TMs, and especially Pb, in the mineral matrix of ore fragments in soils (Mariet et al., 2017b). The endogeics were the only ecological category to bioaccumulate all five TMs studied significantly. In comparison to the anecic species, which create permanent vertical galleries, the horizontal burrowing system of endogeics may retain more pore water and consequently increase the bioavailability of TMs and transfer through cutaneous uptake (Suthar et al., 2008; Vijver et al., 2003). Lastly, various physiological abilities may also explain the contrasted bioaccumulations observed between earthworms belonging to different ecological categories. Thus, digestive physiology may modulate the assimilation efficiencies of different species (Peijnenburg et al., 2012; Piearce, 1978). Moreover, once assimilated, species-specific biochemical strategies may determine the internal fate of TMs and their subcellular fractionation (detoxification and storage, interaction with sites of toxic action, excretion) (Leveque et al., 2013; Morgan and Morgan, 1992; Morgan and Morgan, 1998; Vijver et al., 2006). The physiological processes involved in the contrasted bioaccumulation patterns need further studies since they may explain the responses of earthworms we observed at the community level.

4-2- Community responses to contamination

On the uncontaminated station (MA5), total earthworm density reaches 57 ± 19 ind m^{-2}, which is in the range of data reported for European forests (De Wandeler et al., 2016). The distribution within ecological categories is however different with about 7% epigeic, 34% epianecic, 40% anecic strict, and 19% endogeic, reflecting site-specific conditions of the studied area. As an example, we found *Allolobophora zicsii*, an endemic endogeic earthworm species of the Vosges Mountains. A significant decrease of total earthworm density was observed at the stations impacted by mining waste deposits. At the ecological group level, this decline mainly relies on a strong decrease of endogeic and a near-disappearance of anecic and especially anecic strict, which were not retrieved in the CF28 station. More precisely, the results clearly indicate a relationship between the concentrations of TMs accumulated in earthworm tissues and the decline in the density of endogeic and (epi)anecic. Among the TMs studied, Ag, As, and Pb seem particularly involved with internal concentrations exceeding the toxicity thresholds. Indeed, Luo et al. (2014) estimated Pb LC50 (the concentration causing 50 % mortality), EC10, and EC50 (the concentrations causing 10% and 50% effect) values on the survival and reproduction of the earthworm *Eisenia andrei* at 852, 248, and 484 mg_{Pb} kg^{-1} earthworm tissue, respectively. For As, Bustos et al. (2015) determine EC10, 25 and 50 for

Eisenia fetida response of cocoon production at 38, 47 and 57 mg_{As} kg^{-1}, respectively. Thus, with internal concentrations reaching more than 10,000 and 100 mg kg^{-1} for Pb and As, respectively, these TMs may have cause fitness disturbances (growth, reproduction) at the individual scale and therefore disruptions of the population structure. Toxicity data for Ag and Co for earthworms are, to our knowledge, not available in the literature.

Nevertheless, small populations of earthworms, with particular ecological distribution, are still able to survive even under such heavy exposure to TMs, suggesting potential local adaptation of natural populations. Although no definitive evidence has been clearly demonstrated for earthworms, several recent results suggest that TMs may act as selective pressures in natural populations and that genetic variation exists for genes involved in homeostatic regulation and detoxification of TMs (Anderson et al., 2013; Pauwels et al., 2013; Spurgeon et al., 2011).

Finally, beyond the soil contamination, it is well established that other edaphic factors also influence the incidence of earthworms in the environment (De Wandeler et al., 2016). In the present study, the mining operations carried out on the different sites have also disturbed the soil structure and texture. On CF20, the digging of mining wells led to the accumulation of relatively small amounts of excavated materials in comparison to CF28, an ore dump dating back to the 17th century, where tons of tailings (coarse gravel and sand) have been deposited during the mine exploitation. CF29 has been a site of ore washing operations and is characterized by the accumulation of fine and dense particles forming compacted layers (former decantation basins). These specific soil features may likely complicate the activity of earthworms, especially for deep-burrowing species such as anecic strict which have almost completely disappeared at stations CF28 and CF29.

5- Conclusion

Although literature is full of ecotoxicological studies regarding the effects of recent industrial contamination on earthworms, there is a lack of data regarding legacy impact related to very ancient mining activities. Here, we demonstrated using a passive biomonitoring campaign that even several centuries after their deposits, TMs from mining wastes are still bioavailable for local earthworm populations. The related TM accumulation in earthworm tissues, along with the disturbance of soil structure, may explain the decline observed in earthworm density and the disturbance of the ecological distribution marked by the decrease of endogeic and anecic species. It also represents significant loads of TMs potentially transferable to the higher trophic levels. From a management point of view, this study finally points out the necessity to consider ancient mining or smelting wastes as still currently hazardous materials which should be included in the framework of ecological risk assessment of polluted soils and sites.

Acknowledgements

The authors would like to thank Mickaël Hedde (UMR ECOSYS INRA Versailles) for his help in earthworm identification. We are also grateful to Maxime Mermet, Lorène Roscio, and Coline Beaupuy-Mouret for their help during field work. Financial support was provided by the ADEME, the Région Franche-Comté, the French national program EC2CO-Ecodyn (POLMIN, coord.: F. Gimbert), and the European INTERREG V Oberrhein program “Regio Mineralia” (Coord.: J. Gauthier and P. Fluck, CRESAT, Mulhouse).

Supplementary Data: Figure S1 represents the biomass of earthworms for each ecological group for the four stations. Table S1 gives the model outputs of the relationships between trace metal concentrations in earthworm tissue (mg kg^{-1}) and concentrations in soil.

References

Anderson, C.J., Kille, P., Lawlor, A.J., Spurgeon, D.J., 2013. Life-history effects of arsenic toxicity in clades of the earthworm *Lumbricus rubellus*. Environmental Pollution 172, 200–207.

Bouché, M.B., 1972. Lombriciens de France. Ecologie et Systématique. I.N.R.A. (Annales de Zoologie Ecologie Animale N◦ H.S. 72/2), Paris.

Bouché, M.B., 1977. Stratégies Lombriciennes. Bulletin Ecologie Paris 25, 122–132.

Bustos, V., Mondaca, P., Verdejo, J., Sauvé, S., Gaete, H., Celis-Diez, J.L., Neaman, A., 2015. Thresholds of arsenic toxicity to *Eisenia fetida* in field-collected agricultural soils exposed to copper mining activities in Chile. Ecotoxicology and Environmental Safety 122, 448–454.

Button, M., Koch, I., Reimer, K.J., 2012. Arsenic resistance and cycling in earthworms residing at a former gold mine in Canada. Environmental Pollution 169, 74–80.

De Wandeler, H., Sousa-Silva, R., Ampoorter, E., Bruelheide, H., Carnol, M., Dawud, S.M., Danila, G., Finer, L., Hättenschwiler, S., Hermy, M., Jaroszewicz, B., Joly, F.-J., Müller, S., Pollastrini, M., Ratcliffe, S., Raulund-Rasmussen, K., Selvi, F., Valladares, F., Van Meerbeek, K., Verheyen, K., Vesterdal, L., Muys, B., 2016. Drivers of earthworm incidence and abundance across European forests. Soil Biology & Biochemistry 99, 167–178.

Ernst, G., Zimmermann, S., Christie, P., Frey, B., 2008. Mercury, cadmium and lead concentrations in different ecophysiological groups of earthworms in forest soils. Environmental Pollution 156, 1304–1313.

Ettler, V., 2016. Soil contamination near non-ferrous metal smelters: A review. Applied Geochemistry 64, 56–74.

Fluck, P., 2000. Sainte-Marie-aux-Mines ou Les mines du rêve. Une monographie des mines d'argent. Soultz: Les Editions du Patrimoine Minier.

Fluck, P., 2006. Les mines de plomb, cuivre et argent de la Renaissance ont généré des paysages contrastés. L'exemple de l'Alsace et des Vosges (France de l'Est).

Langdon, C.J., Piearce, T.G., Meharg, A.A., Semple, K.T., 2003. Interactions between earthworms and arsenic in the soil environment: a review. Environmental Pollution 124, 361–373.

Leveque, T., Capowiez, Y., Schreck, E., Mazzia, C., Auffan, M., Foucault, Y., Austruy, A., Dumat, C., 2013. Assessing ecotoxicity and uptake of metals and metalloids in relation to two different earthworm species (*Eiseina hortensis* and *Lumbricus terrestris*). Environmental Pollution 179, 232–241.

Luo, W., Verweij, R.A., van Gestel, C.A.M., 2014. Determining the bioavailability and toxicity of lead contamination to earthworms requires using a combination of physicochemical and biological methods. Environmental Pollution 185, 1–9.

Ma, W.-C., 2004. Estimating heavy metal accumulation in oligochaete earthworms: a meta-analysis of field data. Bulletin of Environmental Contamination and Toxicology 72, 663–670.

Mariet, A.-L., de Vaufleury, A., Bégeot, C., Walter-Simonnet, A.-V., Gimbert, F., 2016. Palaeo-pollution from mining activities in the Vosges Mountains: 1000 years and still bioavailable. Environmental Pollution 214, 575–584.

Mariet, A.-L., Gimbert, F., Bégeot, C., Gauthier, J., Fluck, P., Walter-Simonnet, A.V., 2014. Palaeoenvironmental and actual research on contamination by trace metals on the mining district of Sainte-Marie-aux-Mines, Vosges Mountains. In: Collection Edytem Exploitations minières passées et présentes : impacts environnementaux et sociétaux (in French).

Mariet, A.-L., Pauget, B., de Vaufleury, A., Bégeot, C., Walter-Simonnet, A.-V., Gimbert, F., 2017a. Using bioindicators to assess the environmental risk of past mining activities in the Vosges Mountains (France). Ecological Indicators 75, 17–26.

Mariet, A.-L., Sarret, G., Bégeot, C., Walter-Simonnet, A.-V., Gimbert, F., 2017b. Lead highly available in soils centuries after metallurgical activities. Journal of Environmental Quality. Special Issue: Synchrotron radiation-based methods for environmental biogeochemistry.

Morgan, A.J., Morgan, J.E., 1992. The accumulation and intracellular compartmentation of cadmium, lead, zinc and calcium in two earthworm species (*Dendrobaena rubida* and *Lumbricus rubellus*) living in highly contaminated soil. Histochemistry 75, 269–285.

Morgan, J.E., Morgan, A.J., 1990. The distribution of cadmium, copper, lead, zinc and calcium in the tissues of the earthworm *Lumbricus rubellus* sampled from one uncontaminated and four polluted soils. Oecologia 84, 559–566.

Morgan, J.E., Morgan, A.J., 1998. The distribution and intracellular compartmentation of metals in the endogeic earthworm *Aporrectodea caliginosa* sampled from an unpolluted and a metal-contaminated site. Environmental Pollution 99, 167–175.

Morgan, J.E., Morgan, A.J., 1999. The accumulation of metals (Cd, Cu, Pb, Zn and Ca) by two ecologically contrasting earthworm species (*Lumbricus rubellus* and *Aporrectodea caliginosa*): implications for ecotoxicological testing. Applied Soil Ecology 13, 9–20.

Nahmani, J., Lavelle, P., Lapied, E., van Oort, F., 2003. Effects of heavy metal soil pollution on earthworm communities in the north of France. Pedobiologia 47, 663–669.

Pauwels, M., Frérot, H., Souleman, D., Vandenbulcke, F., 2013. Using biomarkers in an evolutionary context: Lessons from the analysis of biological responses of oligochaete annelids to metal exposure. Environmental Pollution 179, 343–350.

Peijnenburg, W., Capri, E., Kula, C., Liess, M., Luttik, R., Montforts, M., Nienstedt, K., Römbke, J., Sousa, J.P., Jensen, J., 2012. Evaluation of Exposure Metrics for Effect Assessment of Soil Invertebrates. Critical Reviews in Environmental Science and Technology 42, 1862–1893.

Pelosi, C., Bertrand, M., Capoweiz, Y., Boizard, H., Estrade, J. R., 2009. Earthworm collection from agricultural fields: Comparisons of selected expellants in presence/absence of hand sorting. European Journal of Soil Biology 45, 176–183.

Pérès, G., Vandenbulcke, F., Guernion, M., Hedde, M., Beguiristain, T., Douay, F., Houot, S., Piron, D., Richard, A., Bispo, A., Grand, C., Galsomies, L., Cluzeau, D., 2011. Earthworm indicators as tools for soil monitoring, characterization and risk assessment. An example from the national Bioindicator programme (France). Pedobiologia 54S, S77–S87.

Piearce, T.P., 1978. Gut contents of some lumbricid earthworms. Pedobiologia 18, 153–157.

Qiu, H., Peijnenburg, W.J.G.M., van Gestel, C.A.M., Vijver, M.G., 2014. Can commonly measurable traits explain differences in metal accumulation and toxicity in earthworm species? Ecotoxicology 23, 21–32.

Rékási, M., Filep, T., 2015. Factors determining Cd, Co, Cr, Cu, Ni, Mn, Pb and Zn mobility in uncontaminated arable and forest surface soils in Hungary. Environmental Earth Sciences 74, 6805–6817.

R Core Team, 2014. R: A language and environment for statistical computing. R Foundation for Statistical Computing, Vienna, Austria. URL: http://www.R-project.org

Singh, J., Singh, S., Vig, A.P., 2016. Extraction of earthworm from soil by different sampling methods: a review. Environment, Development and Sustainability 18, 1521–1539.

Spurgeon, D.J., Hopkin, S.P., 1996. The effects of metal contamination on earthworm populations around a smelting works – quantifying species effects. Applied Soil Ecology 4, 147–160.

Spurgeon, D.J., Lister, L., Kille, P., Pereira, M.G., Wright, J., Svendsen, C., 2011. Toxicokinetic studies reveal variability in earthworm pollutant handling. Pedobiologia 54S, S217–S222.

Suthar, S., Singh, S., Dhawan, S., 2008. Earthworms as bioindicator of metals (Zn, Fe, Mn, Cu, Pb and Cd) in soils: Is metal bioaccumulation affected by their ecological category? Ecological Engineering 32, 99–107.

Tischer, S., 2009. Earthworms (Lumbricidae) as bioindicators: the relationship between in-soil and in-tissue heavy metal content. Polish Journal of Ecology 57, 513–523.

Tondoh, J.E., Monin, L.M., Tiho, S., Csuzdi, C., 2007. Can earthworms be used as bio-indicators of land-use perturbations in semi-deciduous forest? Biology and Fertility of Soils 43, 585–592.

Tylecote, R.F., 1987. The early history of metallurgy in Europe. Longman archaeology series. London. 391 p.

Vijver, M.G., van Gestel, C.A.M., van Straalen, N.M., Lanno, R.P., Peijnenburg, W.J.G.M., 2006. Biological significance of metals partitioned to subcellular fractions within earthworms (*Aporrectodea caliginosa*). Environmental Toxicology and Chemistry 25, 807–814.

Vijver, M.G., Vink, J.P.M., Miermans, C.J.H., van Gestel, C.A.M., 2003. Oral sealing using glue: a new method to distinguish between intestinal and dermal uptake of metals in earthworms. Soil Biology & Biochemistry 35, 125–132.

Wilson, S.C., Lockwood, P.V., Ashley, P.M., Tighe, M., 2010. The chemistry and behaviour of antimony in the soil environment with comparisons to arsenic: a critical review. Environmental Pollution 158, 1169–1181.

Table captions

Table 1: Concentrations of Ag, As, Cd, Co and Pb (µg g^{-1}) for the four stations for three depths (0-5 cm; 5-15 cm; 15-30 cm). Significant differences of concentrations in soils between stations and depths for a TM were highlighted by different letters.

Table 2: Main habitat descriptors of the four stations.

Table 3: Main representative earthworm species sampled in the four stations and for the four ecological groups.

Table 4: Model outputs of the relationships between earthworm density (ind m^{-2}) and their internal concentrations (mg kg^{-1}). Data are given for whole species (total) and each ecological group. SE = Standard Error. For each metal and each model parameter, different letters indicate significant differences.

Table 1

Station	Depth (cm)	Ag	As	Cd	Co	Pb
MA5	0-5	0.34 ± 0.06 ^{a}	39.97 ± 5.83 ^{a}	0.35 ± 0.04 ^{ab}	29.14 ± 8.21 ^{a}	175.69 ± 24.18 ^{a}
	5-15	0.75 ± 0.04 ^{b}	57.92 ± 10.53 ^{b}	0.29 ± 0.05 ^{ab}	25.93 ± 5.81 ^{a}	357.88 ± 53.64 ^{b}
	15-30	0.14 ± 0.04 ^{c}	36.24 ± 6.24 ^{a}	0.26 ± 0.07 ^{ab}	27.66 ± 4.37 ^{a}	92.37 ± 11.62 ^{c}
CF20	0-5	1.10 ± 0.15 ^{d}	254.89 ± 61.25 ^{c}	0.41 ± 0.08 ^{b}	17.74 ± 2.86 ^{b}	341.63 ± 40.78 ^{b}
	5-15	0.29 ± 0.05 ^{a}	150.02 ± 20.13 ^{d}	0.25 ± 0.04 ^{a}	18.54 ± 3.13 ^{b}	177.64 ± 34.72 ^{a}
	15-30	0.66 ± 0.14 ^{b}	267.89 ± 56.72 ^{c}	0.49 ± 0.11 ^{b}	27.05 ± 6.03 ^{a}	325.52 ± 87.45 ^{b}
CF29	0-5	4.69 ± 1.12 ^{d}	257.85 ± 58.16 ^{c}	1.10 ± 0.38 ^{c}	22.99 ± 7.49 ^{a}	2539.25 ± 374.18 ^{d}
	5-15	60.41 ± 19.15 ^{e}	3110.54 ± 514.36 ^{d}	3.88 ± 0.57 ^{d}	94.05 ± 23.64 ^{c}	22,347.63 ± 2795.78 ^{e}
	15-30	132.23 ± 36.72 ^{f}	3574.07 ± 427.10 ^{d}	8.21 ± 0.95 ^{e}	91.43 ± 8.67 ^{c}	54,048.87 ± 5708.36 ^{f}
CF28	0-5	14.80 ± 1.40 ^{g}	888.25 ± 43.67 ^{e}	1.33 ± 0.10 ^{c}	18.12 ± 1.61 ^{ab}	8582.87 ± 385.3 ^{g}
	5-15	30.50 ± 1.78 ^{h}	1658.30 ± 109.92 ^{f}	2.08 ± 0.18 ^{f}	29.10 ± 3.46 ^{a}	12,153.67 ± 849.09 ^{g}
	15-30	65.79 ± 6.12 ^{e}	2334.15 ± 145.11 ^{g}	3.54 ± 2.13 ^{cdf}	48.72 ± 2.13 ^{d}	24,748.40 ± 3209 ^{e}

Table 2

Station	Altitude (m a.s.l.)	Dominating tree species	pH water	Clay (g kg^{-1})	Silt (g kg^{-1})	Sand (g kg^{-1})	C_{org} (g kg^{-1})	CEC (cmol^{+} kg^{-1})
MA5	730	*Abies alba*, *Acer pseudoplatanus*, *Fagus sylvatica*	4.6 ± 0.1	266 ± 31	286 ± 29	448 ± 59	75.5 ± 7.6	25.7 ± 0.6
CF29	782	*Abies alba*, *Acer pseudoplatanus*	5.0 ± 0.1	99 ± 34	305 ± 139	595 ± 172	19.2 ± 1.6	8.6 ± 1.2
CF28	804	*Abies alba*, *Picea abies*	4.3 ± 0.1	133 ± 13	242 ± 20	625 ± 33	52.3 ± 17.5	15.5 ± 3.4
CF20	856	*Abies alba*, *Fagus sylvatica*	4.7 ± 0.05	131 ± 8	234 ± 21	635 ± 28	27.4 ± 5.1	11.9 ± 1.6

Table 3

Station	Epigeic	Endogeic	Epianecic	Anecic strict
MA5	*Lumbricus moliboeus*	*Allolobophora zicsii* *Aporrectodea caliginosa*	*Lumbricus rubellus rubellus* *Lumbricus rubellus friendoides*	*Aporrectodea* sp.
CF20	*Allolobophora antipai (vogesiana?)*	*Aporrectodea caliginosa* *Aporrectodea longa*	*Lumbricus rubellus rubellus*	*Aporrectodea (nocturna?)*
CF28	*Lumbricus* sp.	*Aporrectodea caliginosa*	*Lumbricus rubellus rubellus*	-
CF29	*Lumbricus* sp.	*Allolobophora rosea vedovinii* *Aporrectodea caliginosa*	*Lumbricus rubellus rubellus*	*Aporrectodea* sp.

Table 4

Metal	Constant	Total			Epigeic			Epianecic			Anecic strict			Endogeic		
		value	SE	*p*-value	value	SE	*p*-value	value	SE	*p*-value	value	SE	*p*-value	value	SE	*p*-value
Ag	d0	1.251	0.108	<0.001	0.723 ^{a}	0.211	0.001	1.517 ^{b}	0.182	<0.001	1.797 ^{ab}	0.639	0.007	1.183 ^{ab}	0.156	<0.001
	-k	-1.721	0.542	0.002	-0.029 ^{a}	1.197	0.981	-3.075 ^{b}	0.734	<0.001	-1.768 ^{ab}	1.306	0.182	-1.890 ^{ab}	0.695	0.009
As	d0	1.518	0.173	<0.001	0.697 ^{a}	0.194	<0.001	2.125 ^{b}	0.359	<0.001	1.999 ^{b}	0.428	<0.001	1.565 ^{b}	0.326	<0.001
	-k	-0.444	0.105	<0.001	0.022 ^{a}	0.189	0.906	-0.733 ^{b}	0.157	<0.001	-0.478 ^{b}	0.179	0.010	-0.557 ^{b}	0.195	0.006
Cd	d0	1.031	0.278	<0.001	0.529 ^{a}	0.306	0.090	3.855 ^{a}	1.837	0.041	0.212 ^{a}	0.209	0.316	0.755 ^{a}	0.432	0.087
	-k	-0.184	0.293	0.533	0.331 ^{a}	0.603	0.586	-2.041 ^{b}	0.694	0.005	1.581 ^{ac}	0.921	0.093	0.076 ^{abc}	0.506	0.880
Co	d0	1.348	0.373	<0.001	0.637 ^{ab}	0.340	0.067	11.03 ^{ab}	7.205	0.132	0.172 ^{a}	0.143	0.233	1.872 ^{b}	0.620	0.004
	-k	-0.644	0.421	0.133	0.175 ^{ac}	0.761	0.819	-4.090 ^{b}	1.104	<0.001	2.488 ^{a}	1.078	0.025	-1.213 ^{c}	0.509	0.022
Pb	d0	2.129	0.359	<0.001	0.805 ^{a}	0.273	0.005	2.151 ^{b}	0.352	<0.001	24.75 ^{ab}	22.78	0.283	2.843 ^{b}	0.898	0.003
	-k	-0.332	0.057	<0.001	-0.039 ^{a}	0.115	0.734	-0.403 ^{b}	0.083	<0.001	-1.152 ^{c}	0.351	0.002	-0.443 ^{bc}	0.122	<0.001

Figure captions

Figure 1: Distribution of individuals in ecological groups, expressed as density (mean ± S.D., individuals m^{-2}). Significant differences of density between stations for an ecological group were highlighted by different letters.

Figure 2: Principal component analysis between earthworm community descriptors (total density and biomass), soil contamination (total Ag, As, Cd, Co, and Pb concentrations) and soil characteristics as texture (sand and silt contents), pH, and OM content. Left: Axis 1 and 2; Right: Axis 1 and 3. Stations (MA5, CF20, CF28 and CF29) are also projected.

Figure 3: Modelled relationships between trace metal concentrations in earthworm tissues (mg kg^{-1}) and concentrations in soil (mg kg^{-1}). (A): Model fitted to the whole data. (B): Models fitted to each ecological group. Details about model outputs for each ecological group are given in Table S2.

Figure 4: Modelled relationships between earthworm density (ind m^{-2}) and trace metal concentrations in their tissues (mg kg^{-1}). The model was fitted to the whole data. Details about model outputs for each ecological group are given in Table 4.

498 **Figure 1**

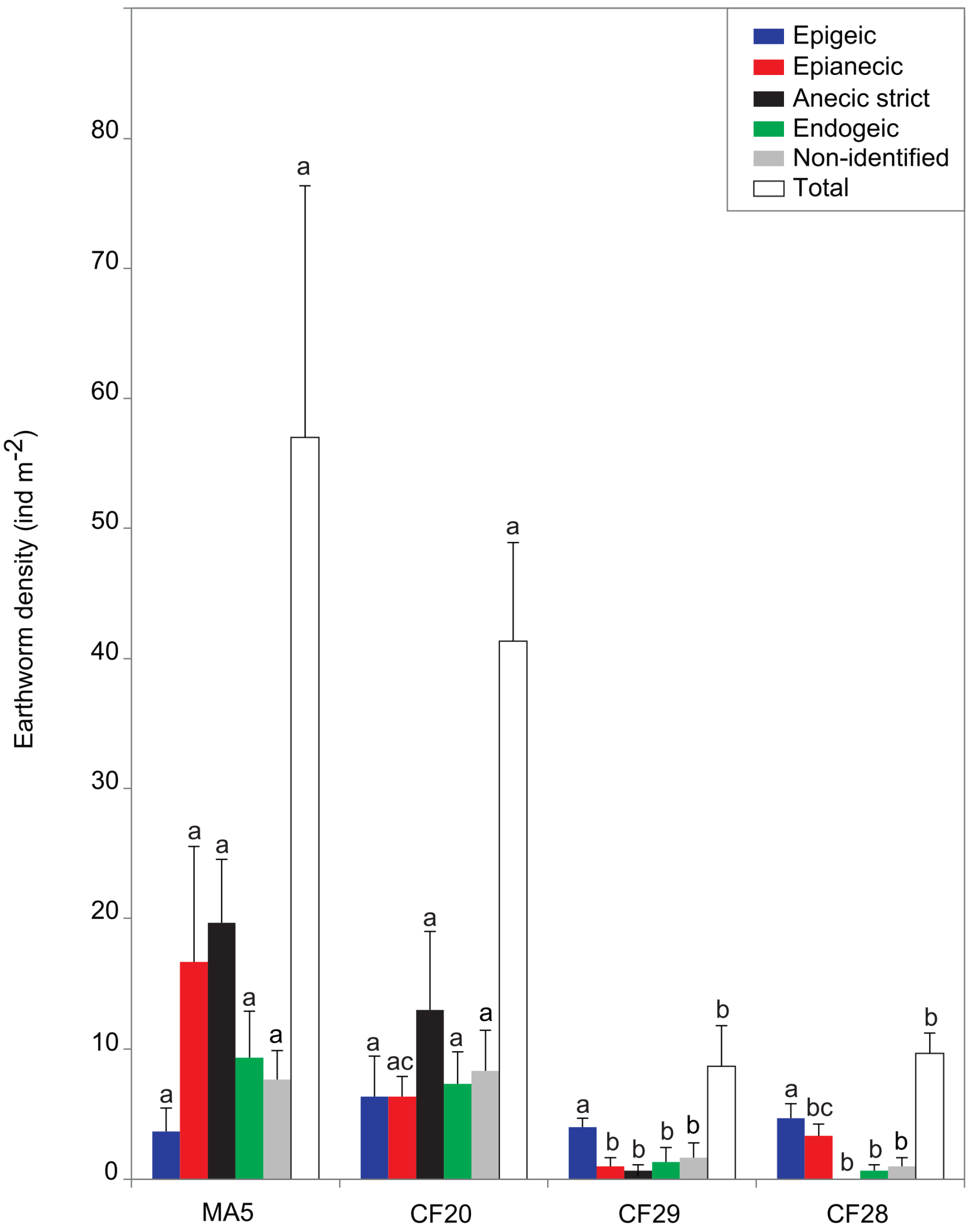

499

500

Figure 2

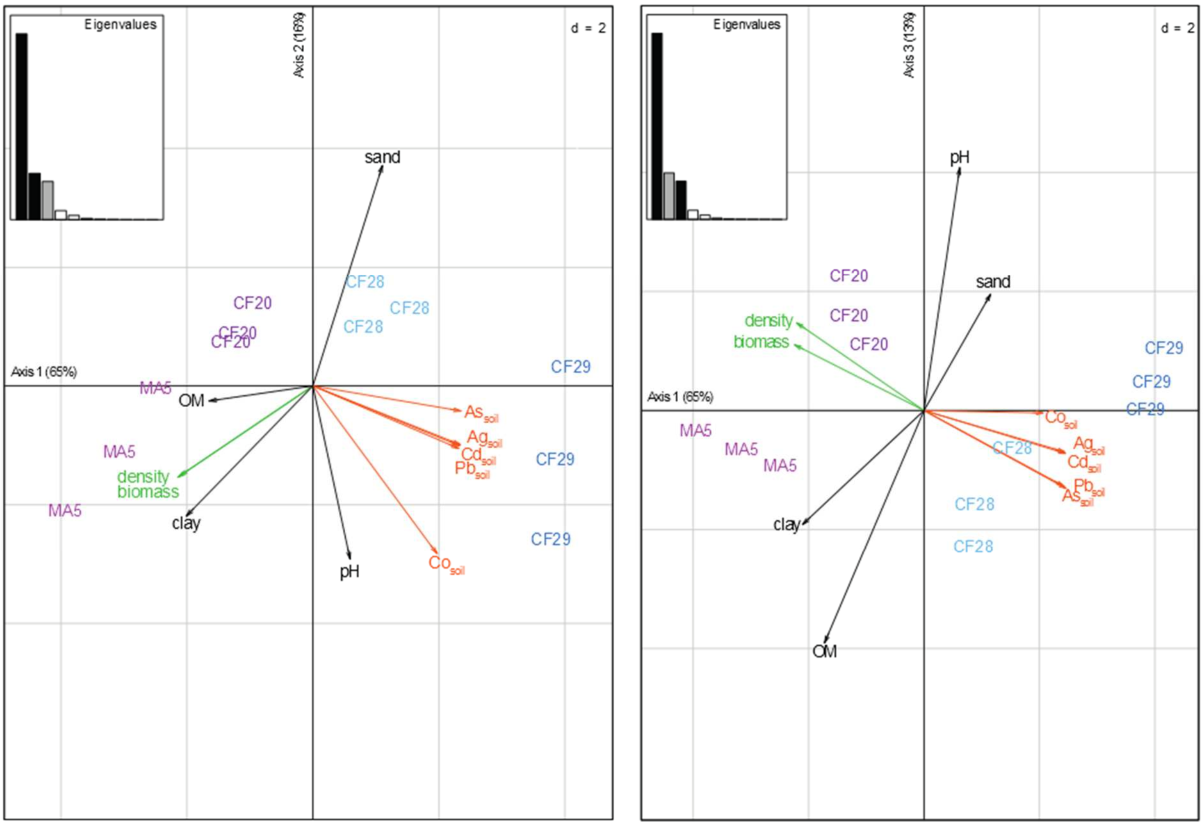
Eigenvalues
Axis 2 (16%)
d = 2
Axis 1 (65%)
sand
CF28
CF20
CF28
CF20
CF28
CF20
CF29
MA5
OM
As_{soil}
Ag_{soil}
Cd_{soil}
Pb_{soil}
MA5
density
biomass
CF29
MA5
clay
CF29
pH
Co_{soil}
Eigenvalues
Axis 3 (13%)
d = 2
pH
CF20
sand
density
CF20
biomass
CF20
CF29
CF29
Axis 1 (65%)
CF29
Co_{soil}
MA5
MA5
CF28
Ag_{soil}
Cd_{soil}
MA5
Pb_{soil}
As_{soil}
CF28
clay
CF28
OM

Figure 3

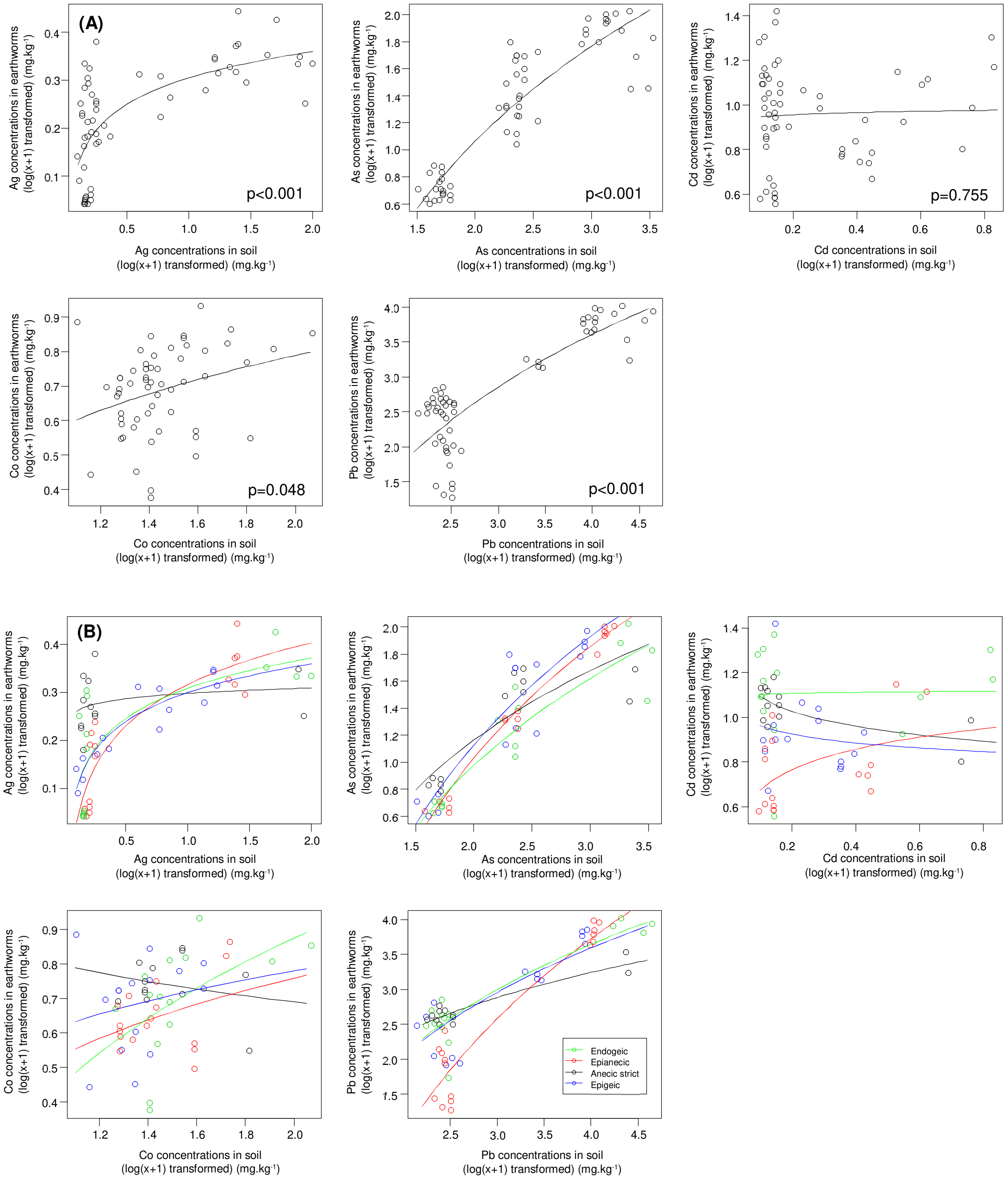
(A)
Ag concentrations in earthworms (log(x+1) transformed) (mg.kg⁻¹)
Ag concentrations in soil (log(x+1) transformed) (mg.kg⁻¹)
p<0.001
As concentrations in earthworms (log(x+1) transformed) (mg.kg⁻¹)
As concentrations in soil (log(x+1) transformed) (mg.kg⁻¹)
p<0.001
Cd concentrations in earthworms (log(x+1) transformed) (mg.kg⁻¹)
Cd concentrations in soil (log(x+1) transformed) (mg.kg⁻¹)
p=0.755
Co concentrations in earthworms (log(x+1) transformed) (mg.kg⁻¹)
Co concentrations in soil (log(x+1) transformed) (mg.kg⁻¹)
p=0.048
Pb concentrations in earthworms (log(x+1) transformed) (mg.kg⁻¹)
Pb concentrations in soil (log(x+1) transformed) (mg.kg⁻¹)
p<0.001
(B)
Ag concentrations in earthworms (log(x+1) transformed) (mg.kg⁻¹)
Ag concentrations in soil (log(x+1) transformed) (mg.kg⁻¹)
As concentrations in earthworms (log(x+1) transformed) (mg.kg⁻¹)
As concentrations in soil (log(x+1) transformed) (mg.kg⁻¹)
Cd concentrations in earthworms (log(x+1) transformed) (mg.kg⁻¹)
Cd concentrations in soil (log(x+1) transformed) (mg.kg⁻¹)
Co concentrations in earthworms (log(x+1) transformed) (mg.kg⁻¹)
Co concentrations in soil (log(x+1) transformed) (mg.kg⁻¹)
Pb concentrations in earthworms (log(x+1) transformed) (mg.kg⁻¹)
Pb concentrations in soil (log(x+1) transformed) (mg.kg⁻¹)
Endogeic
Epianecic
Anecic strict
Epigeic

Figure 4

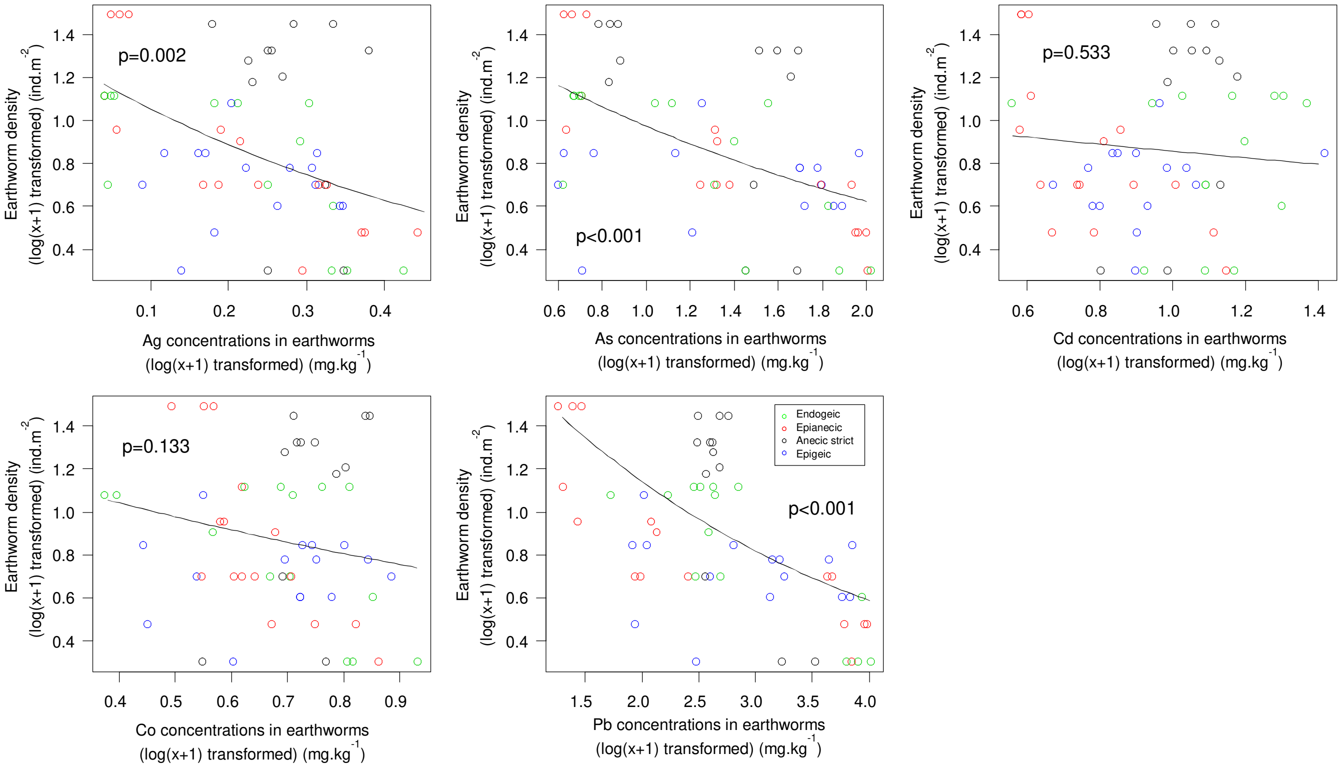

p=0.002
p<0.001
p=0.533
p=0.133
p<0.001
Earthworm density (log(x+1) transformed) (ind.m-2)
1.4
1.2
1.0
0.8
0.6
0.4
0.1
0.2
0.3
0.4
Ag concentrations in earthworms (log(x+1) transformed) (mg.kg-1)
0.6
0.8
1.0
1.2
1.4
1.6
1.8
2.0
As concentrations in earthworms (log(x+1) transformed) (mg.kg-1)
0.6
0.8
1.0
1.2
1.4
Cd concentrations in earthworms (log(x+1) transformed) (mg.kg-1)
0.4
0.5
0.6
0.7
0.8
0.9
Co concentrations in earthworms (log(x+1) transformed) (mg.kg-1)
1.5
2.0
2.5
3.0
3.5
4.0
Pb concentrations in earthworms (log(x+1) transformed) (mg.kg-1)
Endogeic
Epianecic
Anecic strict
Epigeic

Generated compounds at the V-slag/CaO diffusion surface and diffusion characteristics of V and Ca in calcium vanadate

Declarations of interest: none

Hong-Rui Yue [1], Xiang-Xin Xue [1] *

1) School of Metallurgy, Northeastern University, Shenyang 110819, China

Corresponding author: Xiang-Xin Xue; e-mail: xuexx@mail.neu.edu.cn;

Email: Hong-Rui Yue, hongrui.neu@gmail.com;

Xiang-Xin Xue, xuexx@mail.neu.edu.cn;

Abstract

Vanadium slag/CaO diffusion couples were prepared to study the diffusion characteristics of the vanadium slag/CaO interface at 1083 K in the air. The generated phases at different regions were characterized by EPMA, EDS, XRD, and element maps analysis. At the vanadium slag surface that the diffused Ca dose not reached, the main generated phases were Mn_2O_3 and Fe_2O_3. V^{3+} was oxidized to V^{5+} and reacted with the Ca^{2+} to form a small amount of $Ca_2V_2O_7$. Cr was at a disadvantage compared with V in occupying the original Ca^{2+} of the slag. At the vanadium slag surface that the diffused Ca had reached, the main generated phases were $Ca_2V_2O_7$. At the CaO surface, the main generated phases were $Ca_2V_2O_7$ and $Ca_3V_2O_8$. The interdiffusion coefficients were calculated by a new approach that modified from the Boltzmann-Matano method including the determination of the Matano surface, calculation of the integral and differential using the raw data of the concentration profiles. As the molar fraction of Ca was in the range of 0.15 to 0.86, the average interdiffusion coefficient of Ca^{2+} was 2.54×10^{-8} $cm^2\cdot s^{-1}$. The average interdiffusion coefficient of V^{5+} at the V molar fraction of 0.001 to 0.43 was 1.96×10^{-8} $cm^2\cdot s^{-1}$.

keywords: Vanadium slag, calcium roasting, diffusion couple, diffusion coefficient, Boltzmann-Matano method

1. Introduction

Vanadium slag (V-slag) usually refers to the solid slag produced in the converter during smelting the vanadium titanium magnetite. As a byproduct of iron making, V-slag contains a large amount of low-valent V which is often extracted by the process of crushing, iron removal, roasting, leaching, precipitation and calcining, etc. Among these processes, roasting is the first one that mainly involves chemical reactions, which makes it more complicated and essential. The primary purpose of roasting is to oxidize the low-valent V in the V spinels into high-valent V and enrich it in the vanadates that can be leached out. At first, sodium salts were proposed as the additives in roasting V-slag, $NaCO_3$ [1,2], mixture of NaOH and $NaNO_3$ [3], or NaOH [4] react with V-slag to generate water-soluble soluble vanadates which can be leached in aqueous solution. Under the optimal conditions, almost 100% V can be recovered from the V-slag [4]. In recent years, the sodium salts were gradually abandoned in the roasting due to the severe groundwater pollution caused by sodium ions [5], and calcium salts were proposed as the roasting additives.

Zhang [6] studied the process of roasting V-slag powders with CaO powders by thermogravimetric analysis, and the results showed that the V spinels were oxidized and decomposed as the temperature increasing. When the temperature reached 930 K, the oxidized V begun to react with CaO and form calcium vanadates. Cao [7] and Zhang [8] studied the effect of experimental parameters on the V recovery from roasting V-slag powders with CaO powders. The optimal roasting temperature, roasting time, and mass ratio of CaO to V_2O_5 can be inferred as 1123 K, 1.5-2.5 hours, and 0.5-0.7, respectively. The reports about roasting V-slag with CaO are relatively rare, and the research method is limited to simulate the roasting system by mixing the V-slag powders and CaO powders. The species of the generated phases are still controversial, much less the distribution of them around the reaction interface. Therefore, more systematic studies of roasting V-slag with CaO are necessary to carry out, and the research methods that can intuitively reflect the interfacial reaction characteristics should be introduced.

Preparing the diffusion couple is an intuitive way to study the properties of the reaction interface by coupling dissimilar materials [9]. Simulating reaction systems can help in understanding the phase transformations and the growth of intermediate phases by diffusion-controlled processes [10]. Usually, two materials of different compositions are joined at a sharp planar interface and subjected to heat treatment at a fixed elevated temperature [11]. In the present work, the V-slag/CaO diffusion couples were prepared and roasted at 1083 K which summarized from the optimal roasting parameters [6-8]. In addition to characterizing the diffusion interface of the V-slag/CaO diffusion couple, a new method was proposed to determine the Matano surface and calculate the interdiffusion coefficients. The concentration profiles obtained by EPMA can be directly applied to the new method.

2. Experimental

2.1. Materials

Analytical reagent grade CaO was supplied by Sinopharm Chemical Reagent Co., Ltd. V-slag was gathered from HBIS Group ChengSteel Company, and the composition was analyzed by X-ray fluorescence (XRF, ZSX100e, Rigaku, Japan) and listed in Table 1. The CaO powders and V-slag powders were ball-milled by the high energy ball Vario-Planetary Mill (Pulveristte 4, Fritsch, German) for 3 hours. The diameters of CaO powders and V-slag powders were evaluated by field emission scanning electron microscopy (SEM, Ultra Plus, Carl Zeiss GmbH, Jena, Germany) and shown in Fig. 1(a) and Fig. 1(b), respectively. The particle size of CaO and V-slag are distributed around 20 nm and 200 nm, respectively.

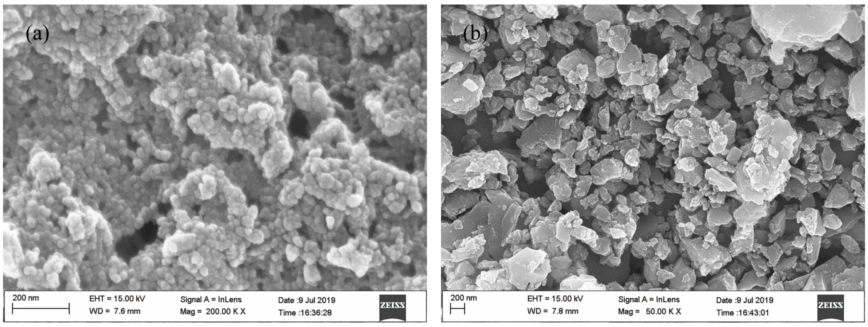

Fig. 1. SEM photographs of CaO particles (a) and raw V-slag particles (b) milled for 3 hours. The ratio of ball to powder was 10:1; the speed of the main-plane and vice-plane were 300 and 150 r/min, respectively; the diameter of the zirconia ball was 10 mm.

Table 1

Chemical composition of the V-slag analyzed by XRF (mass fraction, %)

Fe_2O_3	SiO_2	MnO_2	TiO_2	V_2O_5	MgO	Al_2O_3	CaO	Cr_2O_3
43.4993	14.6256	10.8470	10.2746	8.3874	3.0010	2.6832	2.5803	2.4125

2.2. Preparation of V-slag/CaO diffusion couple

Fig. 2 presents the schematic diagram of preparing the V-slag/CaO diffusion couple. As shown in Fig. 2(a) through Fig. 2(d), the CaO powders were pressed (14130 N) into a pellet of 30 mm diameter and 5 mm thickness in the stainless-steel die. As shown in Fig 2(e) through Fig. 2(h), according to the method [12] that can obtain the dense CaO pellet, here, the CaO pellet was hot-pressed in the graphite die at 1573 K for 120 minutes in the vacuum hot-pressing furnace with the vacuum of 20 Pa. The two circular surfaces of the sintered CaO pellet in Fig. 2(h) were polished using SiC sandpapers (23 μm, 13 μm, and 6.5 μm) with diamond polishing paste (1 μm). As shown in Fig. 2(i) through Fig. 2(l), similar to the embedding method of preparing a diffusion couple [13], here, a quarter of the CaO pellet was embedded into the V-slag powders and pressed (1766 N) into a pellet of 30 mm diameter and 10 mm thickness in a stainless-steel die. As shown in Fig. 2(m) through Fig. 2(p), the V-slag pellet with the CaO pellet were hot-pressed (7065 N) in the graphite die at 1223 K for 90 minutes in the vacuum hot-pressing furnace with the vacuum of 20 Pa. The V-slag/CaO pellet was cut into two pieces, and the diffusion surface was polished using sandpapers and diamond polishing paste. As shown in Fig. 2(q) through Fig. 2(t), the V-slag/CaO diffusion couple was heated to 1083 K and maintained at this temperature for different time in the muffle furnace. The surface directly contacted with the air during the roasting was named *S*(xz). Besides, the graphite die was coated with boron nitride to prevent carbon contamination.

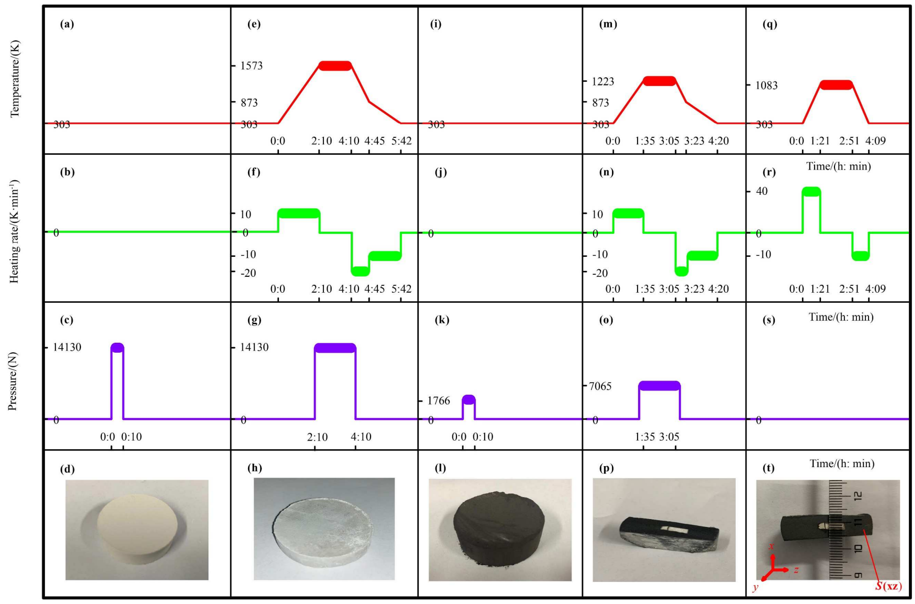

Fig. 2. Schematic diagram of preparing the V-slag/CaO diffusion couple.

2.3. Calculation of interdiffusion coefficients

Fick's second law was proposed to describe the diffusion flux by the concentration gradient and diffusion coefficient [14]. Matano [15] transformed the partial differential equation of Fick's second law [16] to ordinary differential equation utilizing the Boltzmann parameter [17], and suggested using Eq. (1) to determine the variation of the diffusion coefficient with concentration. Eq. (1) which known as the Boltzmann-Matano formula was widely used to calculate the interdiffusion coefficient of the diffusion couple with the initial conditions in Eq. (2) [18]. The integral and differential in Eq. (1) can be graphically expressed by the area (A_{abgf}) and the slope (k) in Fig. 3(a), respectively. Then, the interdiffusion coefficient at a certain concentration (C') can be expressed as Eq. (3). The key to the Boltzmann-Matano method is to find a particular location that satisfies Eq. (4), and this location was named Matano surface [19]. Eq. (4) can be graphically explained as that the area enclosed by C_a, C and the Matano surface equals to that enclosed by C_e, C and the Matano surface. Namely, the critical step is to find the point m on the concentration profiles that makes A_{abm} equals to A_{dem}. However, the concentration profiles of the multiphase materials, such as the V concentration profiles on the V-slag surface in the present work, are always too fluctuant to calculate the integral and differential in Eq. (1). Inspired by the works of Appel [20] and Wagner [21], this paper makes the following modifications to the Boltzmann-Matano method. Firstly, the integral variable in Eq. (4) is changed from dC to dx, and Eq. (4) is expressed as Eq. (5). At the same time, the Riemann integral suggests that the area of a definite integral can be represented by the sum of the areas of the little rectangles. Thus, as shown in Fig. 3(b), the areas defined by C_a, C and the Matano surface (A_{afh}) and C_e, C and the Matano surface (A_{efj}) can be expressed as Eq. (6) and Eq. (7), respectively. As shown in Fig. 3(c), when A_{afh} equals to A_{efj}, the Matano surface (point m) is determined. Secondly, the Matano surface is set as the origin (X=0) of a new X-axis. As shown in Fig. 3(d). A_{abgf} can be expressed as the sum of A_{afh} and A_{hbgf} and calculated as Eq. (8). Thirdly, the slopes are determined numerically using the five-point differentiation formulae [22] as given in Eq. (9) and Eq. (10). Finally, the interdiffusion coefficient can be calculated by Eq. (11). The more information about the new method of calculating the interdiffusion coefficient can be seen in our patent [23].

$$D = -\frac{1}{2t}\frac{\int_{C_a}^{C'} x dC}{\left(\frac{dC}{dx}\right)_{C=C'}} \tag{1}$$

$$C(x,0) = \begin{cases} C_a, & x < 0 \\ C_e, & x > 0 \end{cases} \tag{2}$$

$$D = -\frac{1}{2t}\frac{A_{\mathrm{abgf}}}{k} \tag{3}$$

$$\int_{C_{\mathrm{a}}}^{C_{\mathrm{m}}} x\, dC = -\int_{C_{\mathrm{m}}}^{C_{\mathrm{e}}} x\, dC \tag{4}$$

$$\int_{x_{\mathrm{a}}}^{x_{\mathrm{m}}} C\,\mathrm{d}x = -\int_{x_{\mathrm{m}}}^{x_{\mathrm{e}}} C\,\mathrm{d}x \tag{5}$$

$$A_{\mathrm{afh}} = \sum_{i=a}^{i=f} (C_{\mathrm{a}} - C_{\mathrm{i}})\,\Delta x \tag{6}$$

$$A_{\mathrm{efj}} = \sum_{i=f}^{i=e} (C_{\mathrm{i}} - C_{\mathrm{e}})\,\Delta x \tag{7}$$

$$A_{\mathrm{abgf}} = \begin{cases} \sum_{i=a}^{i=f} (C_{\mathrm{a}} - C_{\mathrm{i}})\,\Delta X + (C_{\mathrm{a}} - C')(0 - X_{\mathrm{C}'}), & X < 0 \\ \sum_{i=f}^{i=e} (C_{\mathrm{i}} - C_{\mathrm{e}})\,\Delta X + (C' - C_{\mathrm{e}})(X_{\mathrm{C}'} - 0), & X > 0 \end{cases} \tag{8}$$

For interior points:

$$k = \frac{1}{12\Delta X}(C_{\mathrm{X}'-2\Delta\mathrm{X}} - 8C_{\mathrm{X}'-\Delta\mathrm{X}} + 8C_{\mathrm{X}'+\Delta\mathrm{X}} - C_{\mathrm{X}'+2\Delta\mathrm{X}}) \tag{9}$$

For end-points:

$$k = \frac{1}{12\Delta X}(-25C_{\mathrm{X}'} + 48C_{\mathrm{X}'+\Delta\mathrm{X}} - 36C_{\mathrm{X}'+2\Delta\mathrm{X}} + 16C_{\mathrm{X}'+3\Delta\mathrm{X}} - 3C_{\mathrm{X}'+4\Delta\mathrm{X}}) \tag{10}$$

$$D = \begin{cases} -\frac{1}{2t}\frac{\sum_{i=a}^{i=f}(C_{\mathrm{a}}-C_{\mathrm{i}})\Delta X+\left(C_{\mathrm{a}}-C'\right)\left(0-X_{\mathrm{C}'}\right)}{\frac{1}{12\Delta X}(C_{\mathrm{X}'-2\Delta\mathrm{X}}-8C_{\mathrm{X}'-\Delta\mathrm{X}}+8C_{\mathrm{X}'+\Delta\mathrm{X}}-C_{\mathrm{X}'+2\Delta\mathrm{X}})}, & X < 0, \text{interior points} \\ -\frac{1}{2t}\frac{\sum_{i=f}^{i=e}(C_{\mathrm{i}}-C_{\mathrm{e}})\Delta X+\left(C'-C_{\mathrm{e}}\right)(\mathrm{X}_{\mathrm{C}'}-0)}{\frac{1}{12\Delta X}\left(C_{\mathrm{X}'-2\Delta\mathrm{X}}-8C_{\mathrm{X}'-\Delta\mathrm{X}}+8C_{\mathrm{X}'+\Delta\mathrm{X}}-C_{\mathrm{X}'+2\Delta\mathrm{X}}\right)}, & X > 0, \text{interior points} \\ -\frac{1}{2t}\frac{\sum_{i=a}^{i=f}(C_{\mathrm{a}}-C_{\mathrm{i}})\Delta X+\left(C_{\mathrm{a}}-C'\right)(0-X_{\mathrm{C}'})}{\frac{1}{12\Delta X}(-25C_{\mathrm{X}'}+48C_{\mathrm{X}'+\Delta\mathrm{X}}-36C_{\mathrm{X}'+2\Delta\mathrm{X}}+16C_{\mathrm{X}'+3\Delta\mathrm{X}}-3C_{\mathrm{X}'+4\Delta\mathrm{X}})}, & X < 0, \text{end-points} \\ -\frac{1}{2t}\frac{\sum_{i=f}^{i=e}(C_{i}-C_{\mathrm{e}})\Delta X+\left(C'-C_{\mathrm{e}}\right)(X_{\mathrm{C}'}-0)}{\frac{1}{12\Delta X}(-25C_{\mathrm{X}'}+48C_{\mathrm{X}'+\Delta\mathrm{X}}-36C_{\mathrm{X}'+2\Delta\mathrm{X}}+16C_{\mathrm{X}'+3\Delta\mathrm{X}}-3C_{\mathrm{X}'+4\Delta\mathrm{X}})}, & X > 0, \text{end-points} \end{cases} \tag{11}$$

Where D is the interdiffusion coefficient ($\mathrm{cm}^2\cdot\mathrm{s}^{-1}$). C is the concentration (g or mol). t is the time (s). x is the location on the x-axis (μm). A is the area (μm^2). k is the slope. X is the location on the

X-axis (μm).

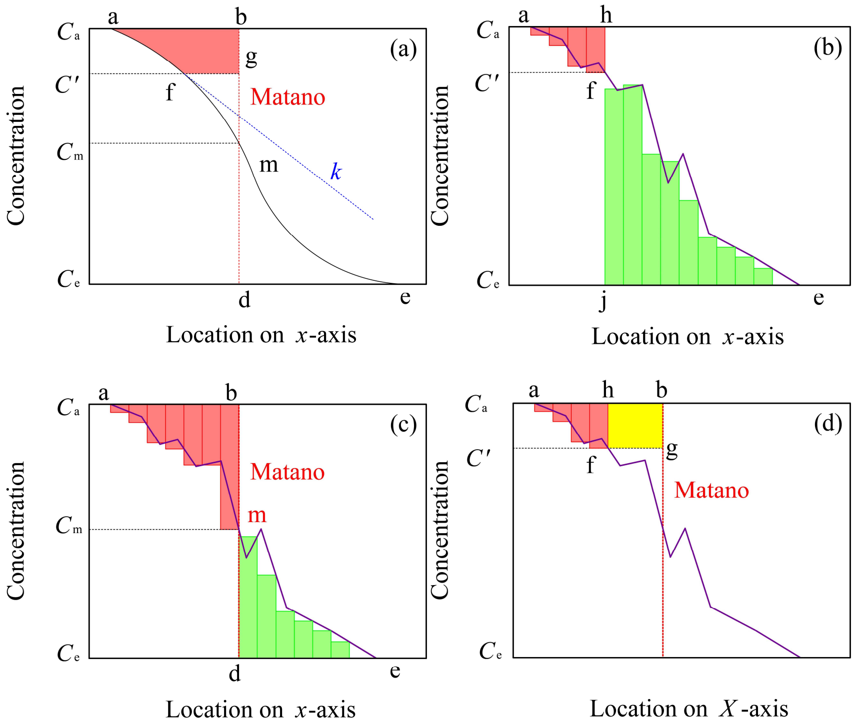

Fig. 3. Graphical interpretation of calculating the interdiffusion coefficient based on the Boltzmann-Matano method.

2.4. Characterization

The diffusion surface sprayed of C was analyzed by the electron probe microanalysis (EPMA, JXA-8530F, JEOL, Japan) with the accelerating voltage of 15 kV. The crystalline phases at different locations on the diffusion surface were identified by the X-Ray diffraction (XRD, SmartLab, Rigaku, Japan) with Cu Kα radiation (λ=1.54056Å), scanning area of 0.5 mm × 0.5 mm, and scanning rate of 5°/min.

3. Results

3.1. The thickness of the transport layer at *S*(xz) before roasting in the air

The cross-sectional views of the diffusion interface before roasting in the air are shown in Fig. 4(a) and 4(b). The red dashed curve and the yellow dashed curve represent the ending diffusion boundary of Ca on the V-slag surface and the ending diffusion boundary of V on the CaO surface, respectively. A narrow transport layer (L_0), 25.5 µm approximately, is presented at the diffusion surface, which means the degree of the reaction between the low-valent V and CaO is very slight. Detecting of concentration by EPMA is performed along the scale line 4-1 in Fig. 4(a) and Fig. 4(b), and the raw data are plotted in Fig. 4(c). From 15 µm to 40 µm, the V profiles show a general downward trend; the Ca profiles present a general upward trend. While, the fluctuating data can also be seen both on the V profiles and Ca profiles, especially that on the V-slag surface. As given in Table 1, the V-slag already contains a small amount of Ca before roasting, and the generated phases after roasting are very complicated. Therefore, it is challenging to precisely determine the ending diffusion boundary of Ca on the V-slag surface by the following SEI-SEM photographs, COMPO-SEM photographs or the concentration profiles.

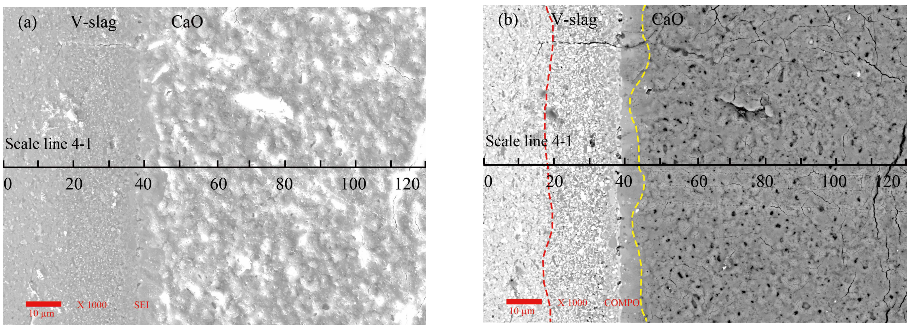

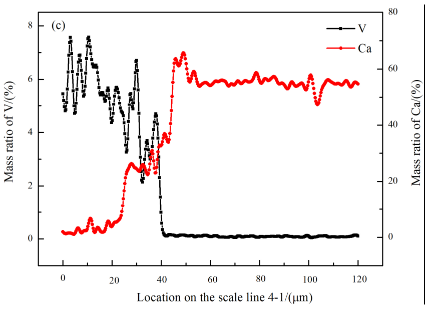

Fig. 4. Cross-sectional views and concentration profiles of the V-slag/CaO interface annealed at 1223 K for 1.5 hours with the vacuum of 20 Pa.

3.2. The diffusion of V and Ca at *S*(xz) roasted in the air with different time

The cross-sectional views of the diffusion interface after roasting in the air for different time and the corresponding concentration profiles are shown in Fig. 5. As illustrated in Fig. 5, the diffusion thickness (L_x) increases with the increase of the roasting time. The diffusion thickness is evaluated by the graphical method [24], and it shows a linear relationship with the square root of roasting time as illustrated in Fig. 6. As usual, three theories were proposed to explain the migration during the diffusion process: the interstitial mechanism [25], the substitutional mechanism [26], and the vacancy mechanism that was widely accepted in metallurgy [27-29]. The vacancy mechanism is that a rise in temperature increases the diffusive mobility of cations; some of them overcome the potential barrier (binding energy in the crystal lattice) and jump [30,31]. The jumped cations diffuse in counter directions toward each other through the cation vacancies and maintain the electrical neutrality at the diffusion interface. The reactions between V_2O_5 and CaO in roasting V-slag were reported [6] as Eqs. (12)-(14). At the same time, the diffusion rate of Ca^{2+} is faster than that of V^{5+} in the calcium vanadates as calculating in the following section. Thus, the reaction mechanism may be that once the V-slag/CaO diffusion couple is heated to the reaction temperature, calcium vanadates begin to form at the V_2O_5/CaO interface. Ca^{2+} diffuses toward V_2O_5 through Ca^{2+} vacancies, and holes (h) diffuse in the counter direction to maintain the electrical neutrality in the calcium vanadates. The diffused Ca^{2+} reacts with V_2O_5 to form calcium vanadates and generate holes at the calcium vanadates/V_2O_5 interface as given in Eqs. (15)-(17).

$$\mathrm{V_2O_5 + CaO = CaV_2O_6} \tag{12}$$

$$\mathrm{V_2O_5 + 2CaO = Ca_2V_2O_7} \tag{13}$$

$$\mathrm{V_2O_5 + 3CaO = Ca_3V_2O_8} \tag{14}$$

$$\mathrm{Ca^{2+} + V_2O_5 + \frac{1}{2}O_2(g) = CaV_2O_6} + 2h \tag{15}$$

$$\mathrm{2Ca^{2+} + V_2O_5 + O_2(g) = Ca_2V_2O_7} + 4h \tag{16}$$

$$\mathrm{3Ca^{2+} + V_2O_5 + \frac{3}{2}O_2(g) = Ca_3V_2O_8} + 6h \tag{17}$$

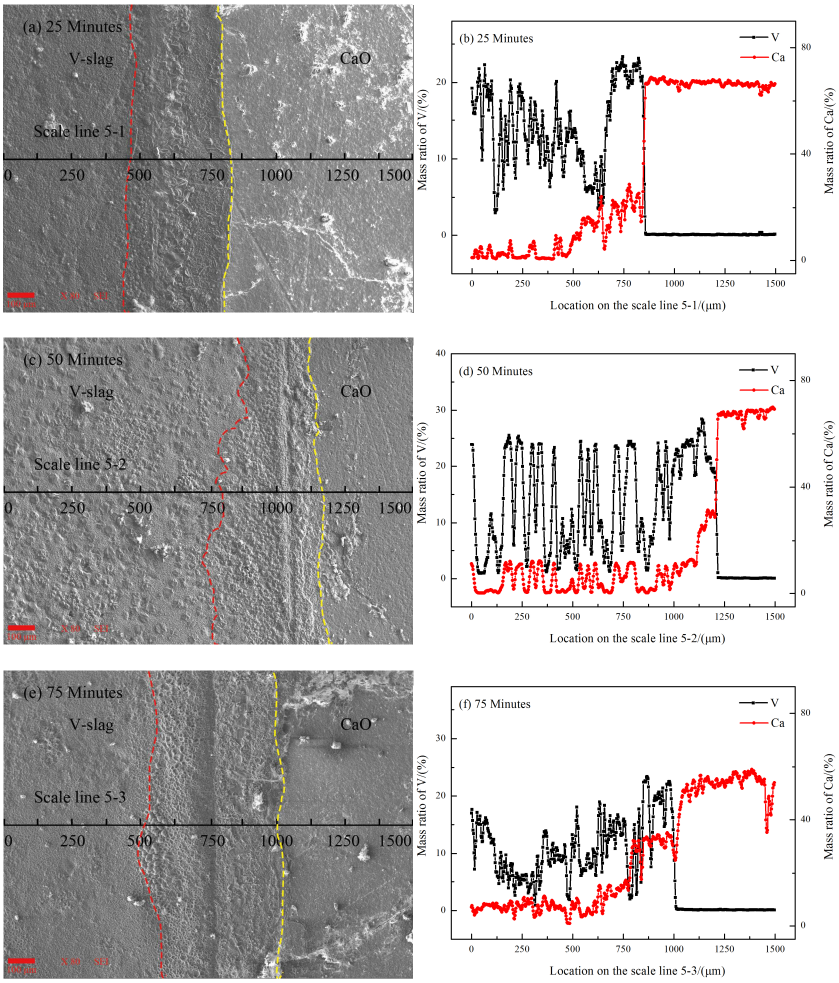

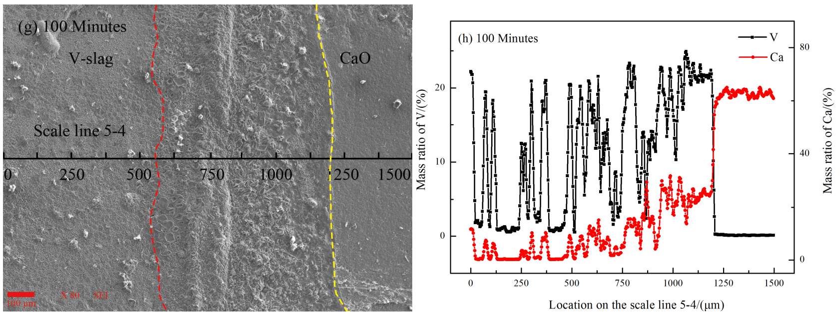

Fig. 5. Cross-sectional views and concentration profiles of the V-slag/CaO interface after annealing at 1083 K in the air for different time.

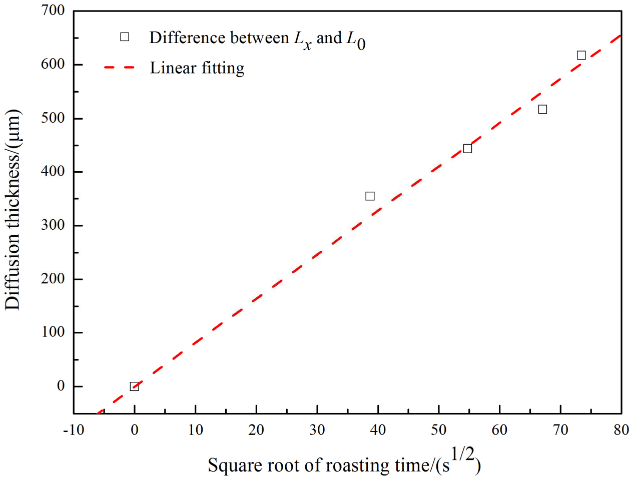

Fig. 6. Relationship between the roasting time and the diffusion thickness at the diffusion surface annealing at 1083 K in the air. The linear fitting coefficient of R^2 is 0.9965.

3.3. Evolution of the main generated compounds with the location at *S*(xz)

Fig. 7 is the phase diagram of the V_2O_5-CaO system from 273 K to 3273 K calculated by the FactSage. As thermodynamic predicting in Fig. 7, three new phases of CaV_2O_6, $Ca_2V_2O_7$ and $Ca_3V_2O_8$ could be formed during annealing at 1083 K. The microscopic characteristics of the *S*(xz) roasted for 75 minutes in the air are shown in Fig. 8(a). The enlarged drawings and EDS analysis of the generated compounds at different locations in Fig. 8(a) are shown in Fig. 8(b), Fig. 8(c), and

Fig. 8(d). As illustrated in Fig. 8(b), the spherical compounds are mainly composed of Mn, Fe, and O with the total mass fraction accounting for 89.07 (regardless of the spraying C). According to the reported XRD analysis [32,33], $(Mn,Fe)(V,Cr)_2O_4$ decomposed during the blank roasting of V-slag, Fe was mainly gathered in Fe_2O_3, Mn was enriched in $Mn_2V_2O_7$. In this case, region 8-1, where the diffused Ca doesn't reach, can also be considered as a blank roasting area. However, the conclusion of quantitative analysis (EDS) in Fig. 8(b) is not the same as the conclusion of qualitative analysis (XRD) in the literature [32], namely, only a small amount of divalent Mn may be gathered into $Mn_2V_2O_7$. Besides, another literature [6] reported that V_2O_5 was preferentially formed calcium vanadates with Ca rather than manganese vanadates with Mn. Only the content of Ca was insufficient could the excess V_2O_5 form manganese vanadates with the divalent Mn which was not oxidized in advance by oxygen. Thus, it can be extracted from the literature [6] and the result in Fig. 8(b) that most of Mn should be preferentially enriched in manganese oxides. As shown in Fig. 8(c), the generated compounds on the V-slag surface and near the V-slag/CaO interface have the bowl-shaped appearance, and the main components are Ca, V, and O that account for 93.67 mass fraction in total. If the oxygen occupied by SiO_2, MgO, P_2O_5, MnO_2, and Fe_2O_3 are excluded, the chemical formula of the generated compounds can be calculated as $Ca_{2.07}V_2O_{5.39}$ which may be the focal calcium vanadate ($Ca_2V_2O_7$) as reported in the literature [6]. It is possible that not all oxides are oxygen-saturated, which would cause too much oxygen has been excluded and lead to less oxygen in $Ca_{2.07}V_2O_{5.39}$ than that in $Ca_2V_2O_7$. As shown in Fig. 8(d), the generated compounds on the CaO surface and near the V-slag/CaO interface have no visible appearance, and the chemical formula is calculated as $Ca_{4.14}V_2O_{9.45}$. The chemical formula can be split as $Ca_2V_2O_7{\cdot}Ca_{2.14}O_{2.45}$ or $Ca_3V_2O_8{\cdot}Ca_{1.14}O_{1.45}$, which indicates the compounds consist of $Ca_2V_2O_7$ and CaO or $Ca_3V_2O_8$ and

CaO or the mixture of $Ca_2V_2O_7$, $Ca_3V_2O_8$ and CaO. This conclusion is consistent with the report [34] that if the temperature is higher than 1023 K and the content of CaO is sufficient, $Ca_2V_2O_7$ and $Ca_3V_2O_8$ may be generated during roasting the V-slag.

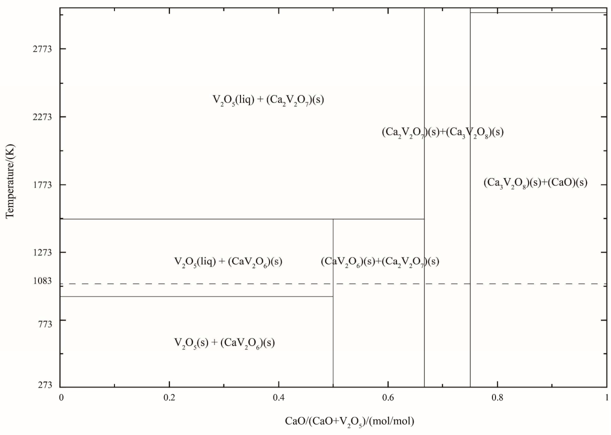

Fig. 7. Phase diagram of the V_2O_5-CaO system calculated by FactSage using the Phase Diagram module.

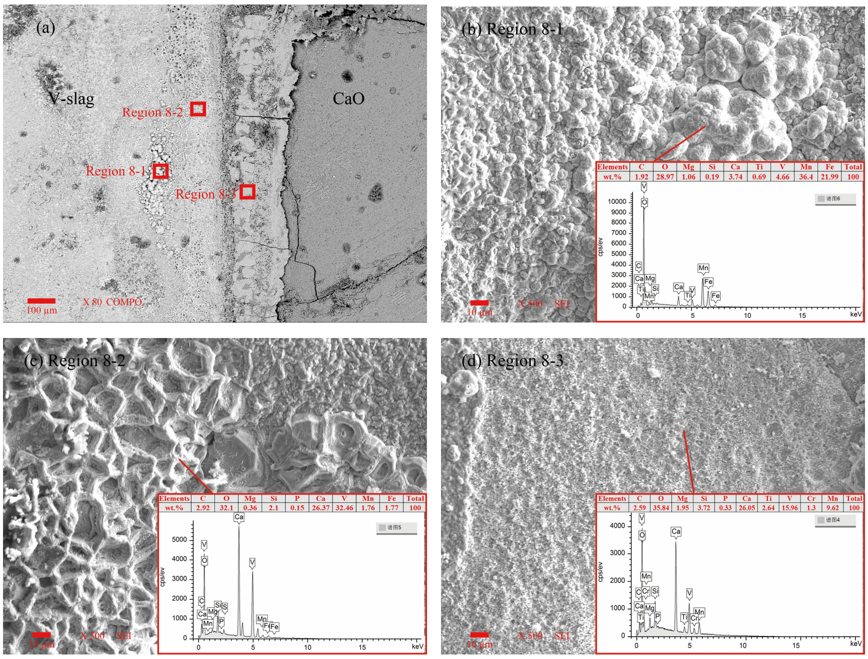

Elements	C	O	Mg	Si	Ca	Ti	V	Mn	Fe	Total
wt.%	1.92	28.97	1.06	0.19	3.74	0.69	4.66	36.4	21.99	100

Elements	C	O	Mg	Si	P	Ca	V	Mn	Fe	Total
wt.%	2.92	32.1	0.36	2.1	0.15	26.37	32.46	1.76	1.77	100

Elements	C	O	Mg	Si	P	Ca	Ti	V	Cr	Mn	Total
wt.%	2.59	35.84	1.95	3.72	0.33	26.05	2.64	15.96	1.3	9.62	100

Fig. 8. Microscopic characteristics and EDS spectra of the generated compounds at different locations on the diffusion surface after annealing at 1083 K in the air for 75 minutes.

The cross-sectional views of the diffusion interface annealed at 1083 K in the air for 75 minutes are shown in Fig. 9(a), the crystal structures of the generated phases at the region 9-1 and region 9-2 are characterized by XRD, and the results are shown in Fig. 9(b). According to Fig. 9(b), the characteristic peaks of $Ca_3V_2O_8$ (JCPDS, 00-039-0090) and $Ca_2V_2O_7$ (JCPDS, 00-028-0836) are observed in the region 9-1, which verifies the EDS analysis in Fig. 8(c) and Fig. 8(d): the main generated compounds around the V-slag/CaO interface are $Ca_3V_2O_8$ and $Ca_2V_2O_7$. The diffraction peaks marked by 4,5 and 6 can be indexed to Fe_2O_3 (JCPDS, 01-089-0597) or $Fe_{1.8966}Mg_{0.1551}O_3$ (JCPDS, 01-070-2674) or Fe_9TiO_{15} (JCPDS, 00-054-1267). The characteristic peaks of Mn_2O_3 (JCPDS, 03-065-7467) are presented in the region 9-2, which verifies the EDS analysis in Fig. 8(b): Mn^{2+} is oxidized into Mn_2O_3 at the V-slag surface where the diffused Ca has not reached. Besides, the diffraction peaks of $CaMn_7O_{12}$ (JCPDS, 01-084-0191) are shown in the region 9-2, and it suggests that some Mn_2O_3 react with CaO and generate $CaMn_7O_{12}$. The diffraction peaks of SiO_2 (JCPDS, 01-079-1912) appears in the region 9-2, which is consistent with the results reported in the literature [32]. It should be noted that CaO (JCPDS, 01-070-4068) also appears in the region 9-2, which may be caused by the limitations of the analyzing equipment. When the 2-theta is 90°, the area of the scanning region (red borders in Fig. 9(a)) is 500 μm × 500 μm. When the 2-theta is less than 90°, the scanning area is greater than 500 μm × 500 μm, and the CaO surface is scanned.

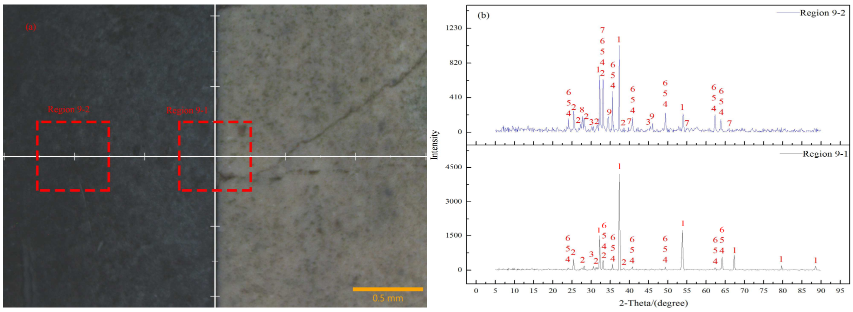

Fig. 9. The cross-sectional views captured by SmartLab (a) and the XRD patterns of the generated

phases at different locations on the diffusion surface (b). 1-CaO; 2- $Ca_3V_2O_8$; 3- $Ca_2V_2O_7$; 4-Fe_2O_3; 5-$Fe_{1.8966}Mg_{0.1551}O_3$; 6-$Fe_9TiO_{15}$; 7-$Mn_2O_3$; 8-$SiO_2$; 9-$CaMn_7O_{12}$.

Fig. 10 shows the cross-sectional views and the elemental maps of the diffusion interface annealed at 1083 K for 5 minutes in the air. The diffusion boundaries marked as the purple dotted curve and the red dotted curve in Fig. 10(a) were determined by the Ca map in Fig. 10(b) and V map in Fig. 10(h). It can be extracted from the EDS analysis that Fe does not diffuse to the CaO surface. Thus, the original interface between V-slag and CaO can be determined by the Fe map in Fig. 10(e) and marked as the gray dotted curve in Fig. 10(a). It can be seen from the three diffusion boundaries that Ca^{2+} diffuses faster than V^{5+} in the generated compounds. As shown in Fig. 10(a), Fig. 10(c), and Fig. 10(h), the regions (region 10-1, region 10-2, and region 10-3) containing primary Mn are only distributed of little V, which confirms the conclusion obtained from the EDS and XRD analysis that most of Mn is enriched into Mn_2O_3 instead of manganese vanadates. As shown in Fig 10(a), Fig. 10(d), Fig. 10(e), and Fig. 10(f), the phase of region 10-4 mainly consists of Fe and O, it should be Fe_2O_3. The phase of region 10-5 mainly consists of Mg, Fe, and O, and it may be $Fe_{1.8966}Mg_{0.1551}O_3$. The phase of region 10-6 mainly consists of Mg and O, and it should be MgO. As shown in Fig. 10(a), Fig. 10(h), and Fig. 10(i), the region 10-7 and region 10-8 contain Cr but do not contain Ca or V. It indicates that Cr is at a disadvantage compared with V when occupying the original Ca in the V-slag, which is consistent with the conclusion in the literature [34]. As shown in Fig. 10(a), Fig, 10(f), and Fig. 10(j), the phase of region 10-9 mainly consists of Si and O, and it may be SiO_2.

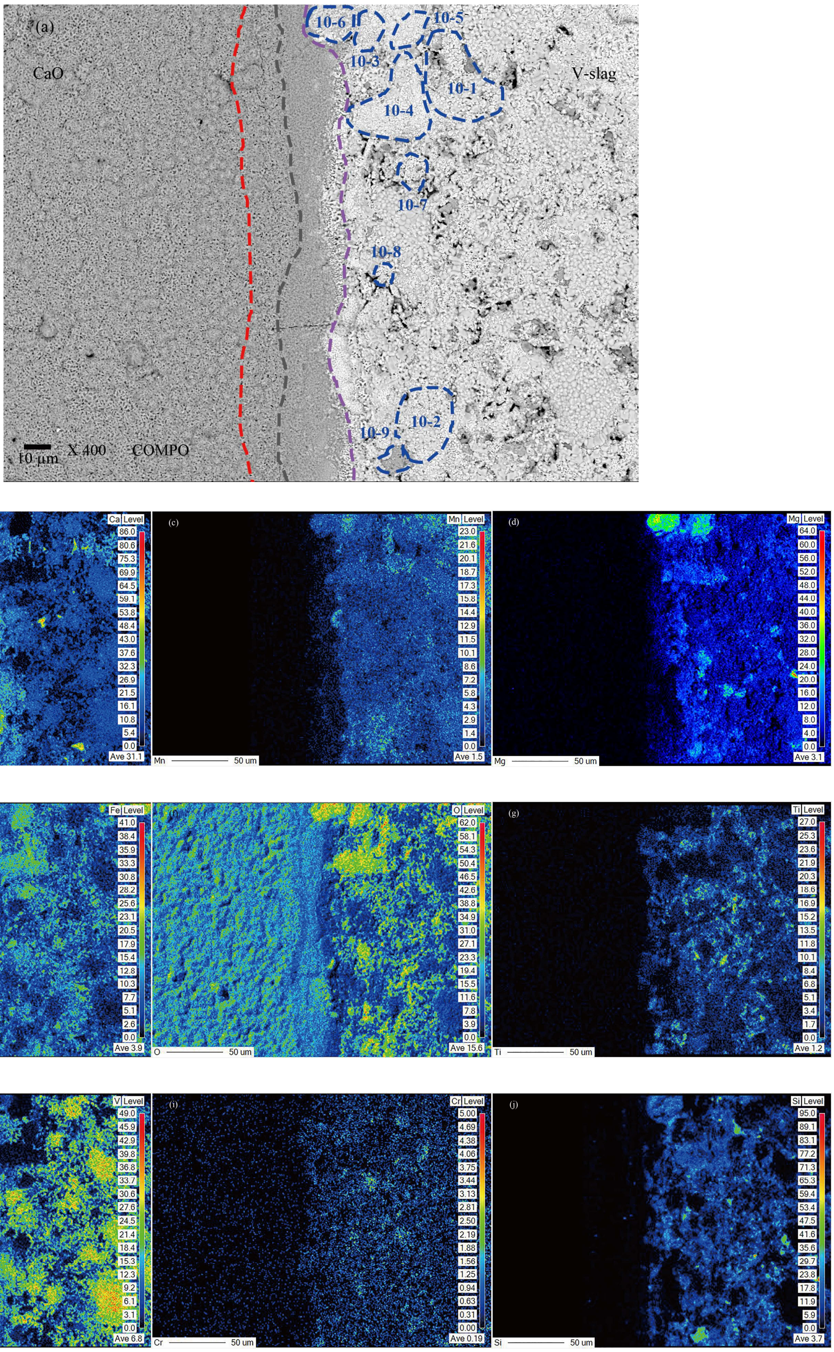

Fig. 10. Cross-sectional views and elements maps of the diffusion interface roasted at 1083 K for 5 minutes in the air.

3.4. Interdiffusion coefficients of Ca^{2+} and V^{5+} in the calcium vanadates

The black solid points in Fig. 11(a) are the raw data of the Ca concentration profiles obtained by EPMA on the scale line 5-3 in Fig. 5. The red and green histograms in Fig. 11(a) are the concentration differences in Eq. (6) and Eq. (7), respectively. The areas (A_{afh} and A_{efj} in Fig. 3) at a location can be calculated as the sum of the areas of the histograms, i.e., the sum of the concentration difference times the scanning step of 2.5 μm. A_{afh} and A_{efj} are shown in Fig. 11(b), and they are closest at 797.5 μm on the scale line 5-3, which indicates 797.5 μm on the scale line 5-3 is the Matano surface. Subsequently, the new X-axis is established with origin of 797.5 μm on the scale line 5-3. A_{hbgf} in Fig. 3(d) is calculated as the product of the concentration difference in Fig. 11(a) and the coordinate on the X-axis, and the data are shown in Fig. 11(c). Finally, A_{abgf} in the Boltzmann-Matano method can be calculated by Eq. (8) and constructed in Fig. 11(d). The slopes of the raw data of the Ca concentration profiles in Fig. 11(a) are calculated by Eq. (9) and Eq. (10) and plotted in Fig. 11(e). If the Ca concentration curve is monotonic, the slopes should all be positive as the concentration increasing with the increase of the coordinates. However, the calculated results show that the slopes in some intervals are negative. Here, the average of the two positive slopes at both ends of the interval is used to replace the negative slopes in the interval. The interdiffusion coefficients of Ca^{2+} ($D_{\mathrm{Ca2+}}$) as a function of the molar fraction of Ca are calculated by Eq. (11) and presented in Fig. 11(f). The $D_{\mathrm{Ca2+}}$ in the generated compounds are substantially in the orders of magnitudes of 10^{-9} to 10^{-7} $\mathrm{cm^2 \cdot s^{-1}}$. If the profiles in Fig. 11(a) are strictly increasing with coordinates, the A_{abgf} in Fig. 11(d) and slope in Fig. 11(e) should increase first and then decrease as the coordinate increasing. However, the volatility of the raw data in Fig. 11(a) causes the fluctuations of the A_{abgf} in Fig. 11(d) and the slope in Fig. 11(e), which also affect the calculated $D_{\mathrm{Ca2+}}$ in Fig. 11(f). As usual, the average of the interdiffusion coefficients in a certain concentration interval was proposed to express the diffusion ability [35-37]. In this case, the average of $D_{\mathrm{Ca2+}}$ with the Ca molar fraction of

0.15-0.86 is calculated as 2.54×10^{-8} cm^{2}·s^{-1}. Besides, the average of D_{Ca2+} calculated by Eq. (11) and the other method [24, 38-40] provided in the literature are listed in Table 2. As given in Table 2, the average of D_{Ca2+} calculated by Eq. (11) is in agreement with that calculated by the method reported in the literature [38]. At the same time, the average of D_{Ca2+} in the calcium vanadates is also in the same order of magnitude as that in the $Ca_2Fe_2O_5$ [24]. These results indicate that the method of calculating the interdiffusion coefficient in this paper is reliable. Similarly, the data generated during the calculation of the interdiffusion coefficients using the V concentration profiles are plotted in Fig. 12. The average of the interdiffusion coefficients of V^{5+} with the V molar fraction of 0.001 to 0.43 is 1.96×10^{-8} cm^{2}·s^{-1}. It can be extracted from the calculated results that the diffusion of Ca^{2+} is faster than the diffusion of V^{5+} in the calcium vanadates, and the calcium vanadates are mainly formed on the V-slag surface. Thus, when roasting the V-slag powders with CaO powders, the particle size of the V-slag should be greater than that of CaO.

Table 2

Interdiffusion coefficients of Ca^{2+} calculated in the present work and the literature [24,38]

Condition	System	Profiles	Method	Medium	$D_{average}$
1083 K	V-slag/CaO	Fig. 5(f)	Eq. (11)	$Ca_2V_2O_7$, $Ca_3V_2O_8$	2.54×10^{-8} cm^{2}·s^{-1}
1083 K	V-slag/CaO	Fig. 5(f)	Reference [38]	$Ca_2V_2O_7$	5.2×10^{-8} cm^{2}·s^{-1}
1173 K	CaO/FeO	Reference [24]	Reference [24]	$Ca_2Fe_2O_5$	2.0×10^{-8} cm^{2}·s^{-1}

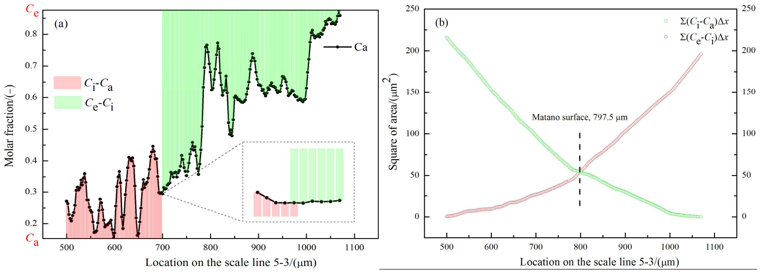

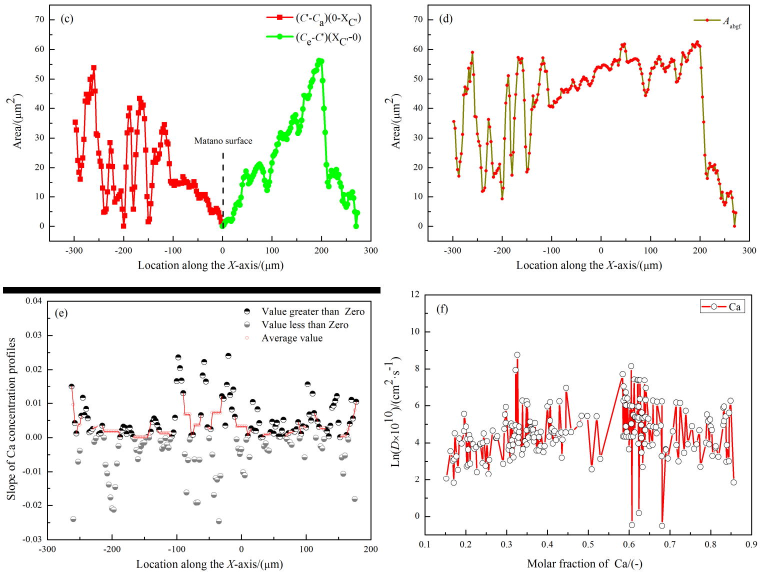

Fig. 11. Calculated data of determining the Matano surface, integral, differential, and the interdiffusion coefficient by the concentration profiles of Ca.

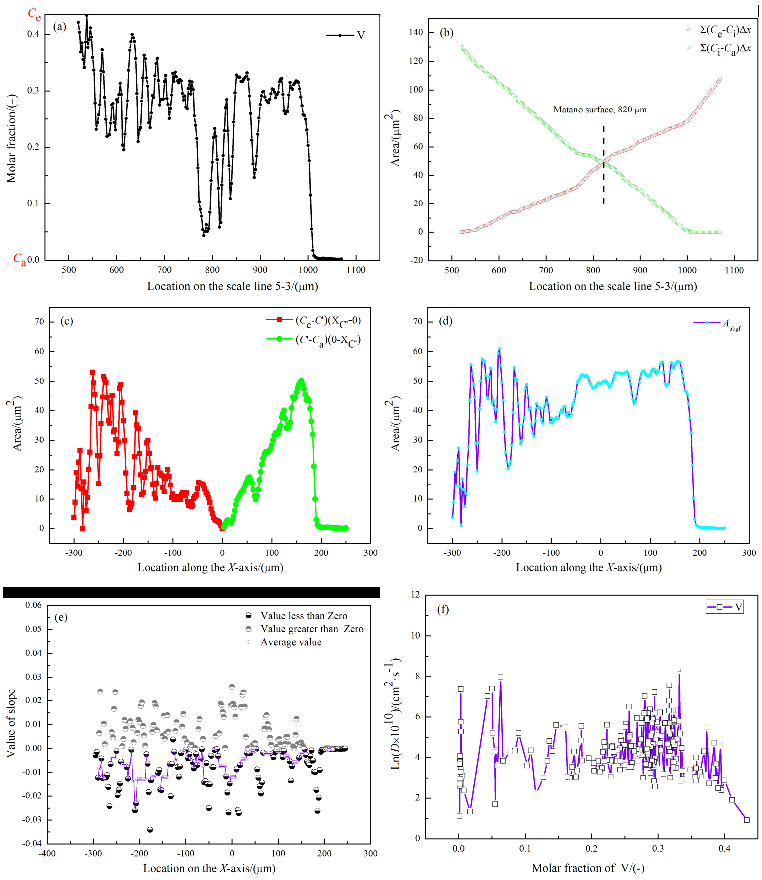

Fig. 12. Calculated data of determining the Matano surface, integral, differential, and the interdiffusion coefficient by the concentration profiles of V.

4. Conclusion

In this paper, the V-slag/CaO diffusion couple was prepared by the vacuum hot-pressing method, and the diffusion experiment was carried out at 1083 K in the air in the muffle furnace. Although the V-slag/CaO diffusion couple can be assembled by the method in this paper, it will start cracking after being stored in a vacuum oven for 1-2 weeks. Therefore, the key to study the diffusion couple containing CaO is to prepare the diffusion couple that will not crack at high temperatures and not deliquesce at low temperatures. Also, the concentration profiles on the V-slag surface are too fluctuant to directly apply in the Boltzmann-Matano method to calculate the interdiffusion coefficient. In this paper, a new method is proposed to determine the Matano surface and calculate the interdiffusion coefficients without smoothing the concentration profiles. According to the result of this paper and related literature, the following conclusions can be used as a reference for the readers.

1. The diffusion thickness of the calcium vanadates is generally proportional to the square root of the roasting time.

2. At the V-slag surface where the diffused Ca has not reached, Fe and Mn are mainly enriched in the corresponding oxides after decomposing from the spinels. The low-valent V is oxidized and reacted with the original Ca in the V-slag to form $Ca_2V_2O_7$. Cr is at a disadvantage of occupying the original Ca in the V-slag comparing with V.

3. At the V-slag surface where the diffused Ca is already reached, the main generated phase is $Ca_2V_2O_7$.

4. At the CaO surface, the main generated phases may be the combination of $Ca_2V_2O_7$ and $Ca_3V_2O_8$.

5. The diffusion coefficient of Ca^{2+} in calcium vanadates is greater than that of V^{5+}, which indicates that calcium vanadates are mainly formed on the V-slag surface. Thus, the size of the V-slag particle should be larger than that of CaO particle in the practice roasting.

Acknowledgment

This work was financially supported by the National Science Foundation of China (Nos. 51674084 and U1502273) and the Fundamental Research Funds for the Central Universities (No. 182503035).

Reference

[1] H.Y. Li, H.X. Fang, K. Wang, W. Zhou, Z. Yang, X.M. Yan, W.S. Ge, Q.W. Li, B. Xie, Asynchronous extraction of vanadium and chromium from vanadium slag by stepwise sodium roasting-water leaching, Hydrometallurgy 156 (2015) 124-135. https://doi.org/10.1016/j.hydromet.2015.06.003

[2] W.C. Song, K. Li, Q. Zheng, H. Li, A novel process of vanadium extraction from molten vanadium bearing slag, Waste Biomass Valori. 5(3) (2014) 327-332. https://doi.org/10.1007/s12649-013-9286-z

[3] A.J. Teng, X.X. Xue, A novel roasting process to extract vanadium and chromium from high chromium vanadium slag using a $NaOH-NaNO_3$ binary system, J. Hazardous Mater. 379 (2019). https://doi.org/10.1016/j.jhazmat.2019.120805

[4] Y.L. Ji, S.B. Shen, J.H. Liu, Y. Xue, Cleaner and effective process for extracting vanadium from vanadium slag by using an innovative three-phase roasting reaction, J. Clean. Prod. 149 (2017) 1068-1078. https://doi.org/10.1016/j.jclepro.2017.02.177

[5] E.I.L. Silva, A. Shimizu, H. Matsunami, Salt pollution in a Japanese stream and its effects on

water chemistry and epilithic algal chlorophyll-a, Hydrobiologia 437(1-3) (2000) 139-148. https://doi.org/10.1023/a:1026598723329

[6] J.H. Zhang, W. Zhang, L. Zhang, S.Q. Gu, Mechanism of vanadium slag roasting with calcium oxide, Int. J. Miner. Process. 138 (2015) 20-29. https://doi.org/10.1016/j.minpro.2015.03.007

[7] P. Cao, X.L. Yang, Y. Peng, Z.B. Fu, L. Chen, Research on the mechanism of producing calcium vanadate, Advanced Materials Research 581-582 (2012) 996-1001. https://doi.org/10.4028/www.scientific.net/AMR.581-582.996

[8] J.H. Zhang, W. Zhang, Z.L. Xue, Oxidation kinetics of vanadium slag roasting in the presence of calcium oxide, Min. Proc. Ext. Met. Rev. 38(5) (2017) 265-273. https://doi.org/10.1080/08827508.2017.1289197

[9] C.J. Li, Z.J. Yuan, R. Guo, W.D. Xuan, Z.M. Ren, Y.B. Zhong, X. Li, H. Wang, Q.L. Wang, Reaction diffusion in Ni-Al diffusion couples in steady magnetic fields, J. Alloy. Comp. 641 (2015) 7-13. https://doi.org/10.1016/j.jallcom.2015.04.061

[10] Z.S Ren, X.J. Hu, X.X. Xue, K.C. Chou, Solid state reaction studies in Fe_3O_4-TiO_2 system by diffusion couple method, J. Alloy. Comp. 580 (2013) 182-186. https://doi.org/10.1016/j.jallcom.2013.05.114

[11] Y. Zhou, Q.Wang, D.L.Sun, X.L.Han, Co-effect of heat and direct current on growth of intermetallic layers at the interface of Ti-Ni diffusion couples, J. Alloy. Comp. 509 (2011) 1201-1205. https://doi.org/10.1016/j.jallcom.2010.09.182

[12] I.B. Bashir, Mechanisms of densification during the hot pressing of calcium oxide and synthetic doloma, Material Science & Engineering 61(1) (1983) 51-57. https://doi.org/10.1016/0025-5416(83)90125-8

[13] M. Peiteado, A.C. Caballero, D. Makovec, Diffusion and reactivity of ZnO-MnO$_x$ system, J. Solid State Chem. 180(9) (2007) 2459-2464. https://doi.org/10.1016/j.jssc.2007.07.001

[14] K.P. Chao, P. Wang, Y.T. Wang, Diffusion and solubility coefficients determined by permeation and immersion experiments for organic solvents in HDPE geomembrane, J. Hazardous Mater. 142 (2007) 227-235. https://doi.org/10.1016/j.jhazmat.2006.08.022

[15] C. Matano, On the relation between the diffusion-coefficients and concentrations of solid metals (the nickel-copper system), Jpn. J. Phys. 8 (1993), 109-113.

[16] A. Fick, Ueber diffusion, Ann. Phys. 170 (1855) 59-86. https://doi.org/10.1002/andp.18551700105

[17] L. Boltzmann, Zur Integration der diffusionsgleichung bei variabeln diffusions-coefficienten, Ann. Phys. 289 (1894) 959-964. https://doi.org/10.1002/andp.18942891315

[18] P.J. Tumidajski, G.W. Chan, R.F. Feldman, G. Strathdee, A Boltzmann-Matano analysis of chloride diffusion, Cement Concrete Res. 25(7) (1995) 1556-1566. https://doi.org/10.1016/0008-8846(95)00149-7

[19] M.A. Dayananda, Determination of eigenvalues, eigenvectors, and interdiffusion coefficients in ternary diffusion from diffusional constraints at the Matano plane, Acta Mater. 129 (2017) 474-481. https://doi.org/10.1016/j.actamat.2017.03.012

[20] M. Appel, Solution for Fick's 2nd law with variable diffusivity in a multi-phase system, Scr. Metall. 2(4) (1967) 217-221. https://doi.org/10.1016/0036-9748(68)90231-7

[21] C. Wagner, The evaluation of data obtained with diffusion couples of binary single-phase and multiphase systems, Acta Metall. 17(2) (1969) 99-107. https://doi.org/10.1016/0001-6160(69)90131-X

[22] C. Heiligers, C.J. Pretorius, J.H. Neethling, Interdiffusion of hafnium carbide and titanium carbide during hot-pressing, Int. J. Refract. Met. H. 31 (2012) 51-55. https://doi.org/10.1016/j.ijrmhm.2011.09.005

[23] H.R Yue, X.X Xue, China Patent, No.CN110263292A (2019).

[24] H. Fukuyama, K. Hossain, K. Nagata, Solid-state reaction kinetics of the system CaO-FeO, Metall. Mater. Trans. B 33(2) (2002) 257-264. https://doi.org/10.1007/s11663-002-0010-9

[25] W.W. Sun, H. Ehteshami, P.R.C. Kent, P.A. Korzhavyi, Self-diffusion of Ti interstitial based point defects and complexes in TiC, Acta Mater. 165 (2019) 381-387. https://doi.org/10.1016/j.actamat.2018.11.056

[26] X.W. Zhou, R.E. Jones, J. Gruber, Molecular dynamics simulations of substitutional diffusion, Comp. Mater. Sci. 128 (2017) 331-336. https://doi.org/10.1016/j.commatsci.2016.11.047

[27] Z.P. Lin, L.L. Bai, X. Zhang, H.F. Dong, F.G. Wu, Na-vacancies-induced magnetism in Na_xMnO_2, J. Magn. Magn. Mater. 468 (2018) 164-167. https://doi.org/10.1016/j.jmmm.2018.08.009

[28] K.N. Goswami, A. Mottura, A kinetic monte carlo study of vacancy diffusion in non-dilute Ni-Re alloys, Mat. Sci. Eng. A-Struct. 743 (2019) 265-273. https://doi.org/10.1016/j.msea.2018.11.064

[29] Z.S. Mi, L. Chen, C.M. Shi, Y. Ma, D.C. Wang, X.L. Li, H.M. Liu, L.J. Qiao, The effects of strain and vacancy defects on the electronic structure of Cr_2O_3, Comp. Mater. Sci. 144 (2018) 64-69. https://doi.org/10.1016/j.commatsci.2017.12.012

[30] K.J. Relmasira, A.Yu. Leonov, P.I. Malenko, Application of molecular dynamics method for

simulation of the process of increasing the diffusion mobility, Procedia Engineering 206 (2017) 636-641. https://doi.org/10.1016/j.proeng.2017.10.529

[31] S.A. Kislenko, M.S. Vlaskin, A.Z. Zhuk, Diffusion of cation impurities by vacancy mechanism in α-Al_2O_3: Effect of cation size and valence, Solid State Ionics 293 (2016) 1-6. https://doi.org/10.1016/j.ssi.2016.05.021

[32] X.F. Zhang, F.G. Liu, X.X. Xue, T. Jiang, Effects of microwave and conventional blank roasting on oxidation behavior, microstructure and surface morphology of vanadium slag with high chromium content, J. Alloy. Compd. 686 (2016) 356-365. https://doi.org/10.1016/j.jallcom.2016.06.038

[33] X.S. Li, B. Xie, Extraction of vanadium from high calcium vanadium slag using direct roasting and soda leaching, Int. J. Min. Met. Mater. 19(7) (2012) 595-601. https://doi.org/10.1007/s12613-012-0600-8

[34] T. Jiang, J. Wen, M. Zhou, X.X Xue, Phase evolutions, microstructure and reaction mechanism during calcification roasting of high chromium vanadium slag, J. Alloy. Compd. 742 (2018), 402-412. https://doi.org/10.1016/j.jallcom.2018.01.201

[35] L.R. Ram-Mohan, M.A. Dayananda, A transfer matrix method for the calculation of concentrations and fluxes in multicomponent diffusion couples, Acta Mater. 54(9) (2006) 2325-2334. https://doi.org/10.1016/j.actamat.2006.01.021

[36] P. Zhang, T. Debroy, S. Seetharaman, Interdiffusion in the MgO-Al_2O_3 spinel with or without some dopants, Metall. Mater. Trans. A 27(8) (1996) 2105-2114. https://doi.org/10.1007/BF02651865

[37] Y. Yuan, Y.Y. Guan, D.J. Li, N. Moelans, Investigation of diffusion behavior in Cu-Sn solid

state diffusion couples, J. Alloy. Comp. 661 (2016) 282-293. https://doi.org/10.1016/j.jallcom.2015.11.214

[38] K. Kawamura, A. Saiki, T. Maruyama, K. Nagata, Diffusion coefficient of yttrium ion in $YCrO_3$, J. Electrochem. Soc. 142(9) (1995), 3073-3077. https://10.1149/1.2048690

[39] C. Wagner, Investigations on silver sulfide, J. Chem. Phys. 21(10) (1953) 1819-1827. https://doi.org/10.1063/1.1698670

[40] T. Maruyama, K. Kawamura, A. Saiki, K. Nagata, Thermodynamics and diffusivity of yttrium in yttrium chromite ($YCrO_3$), Key. Eng. Mater. 111-112 (1995) 303-320. https://doi.org/10.4028/www.scientific.net/kem.111-112.30

Appendix

The meaning of the symbols are lisetd in Table A1.

Table A1. Descriptions of the mainly symbols

S	Surface
S(xz)	Surface parallel to the *x*-axis and *z*-axis
x	Location on the *x*-axis
x_a	Location of initial concentration
x_e	Location of initial concentration
x_m	Location of Matano surface
X	Location on the *X*-axis
X'	Location at a particular concentration
C	Concentration
C_a	Initial concentration
C_e	Initial concentration
C_m	Concentration of Matano surface
C'	Concentration at a particular location
$C_{\mathrm{X}'-2\Delta\mathrm{X}}$	Concentration at X'-$2\Delta X$
$C_{\mathrm{X}'-\Delta\mathrm{X}}$	Concentration at X'-ΔX
$C_{\mathrm{X}'+\Delta\mathrm{X}}$	Concentration at $X'+\Delta X$
$C_{\mathrm{X}'+2\Delta\mathrm{X}}$	Concentration at $X'+2\Delta X$
A	Area
A_abgf	Area enclosed by points a, b, g, and f
A_abm	Area enclosed by points a, b, and m
A_dem	Area enclosed by points d, e, and m
A_afh	Area enclosed by points a, f, and h
A_efj	Area enclosed by points e, f, and j
A_hbgf	Area enclosed by points h, b, g, and f
D	Interdiffusion coefficient
D_average	Average of interdiffusion coefficient
k	Slope
L_0	Diffusion thickness before roasting
L_x	Diffusion thickness after roasting on the *x*-axis
t	Time

Relative error of the calculated interdiffusion coefficient (σ_D/D).

The following Eq.(A1) is deduced from the logarithm of the Boltzmann-Matano formula. According to Eq. (A2) and the propagation of error. The relative error of D can be expressed by the relative errors of *A* and *k* in Eq. (A3) and Eq. (A4), where the relative error of time is assumed to be zero. According to Eq. (8) and the propagation of error, Eq. (A5) and Eq. (A6) are proposed to calculate the relative error of *A*. In the sight of Eq. (9) and Eq. (10), the relative error of *k* can be described by Eq. (A7) and Eq. (A8). Finally, the relative error of *D* can be calculated as the function of the relative error of *C* (0.01) as given in Eq. (A9). The relative errors of *D* at different concentrations are constructed in Fig. A1. In Fig. A1, the relative errors increase sharply as the concentrations closing to the initial concentrations. When the concentrations reach the initial concentrations gradually, the concertation gradient gradually decreases to zero, which lead to the sharply increasing of the relative errors in Eq. (A9). The relationship between the relative error and concentration reflects the limitation of the calculating method in the present work, that is, the calculated interdiffusion coefficients closed to the initial concentrations may have large relative errors.

$$LnD = Ln(-\frac{1}{2t}\frac{A}{k}) \tag{A1}$$

$$\frac{\sigma_{\mathrm{D}}}{D} \approx \frac{dD}{D} = \mathrm{d}LnD \tag{A2}$$

$$\frac{\sigma_{\mathrm{D}}}{D} = \left|-\frac{1}{2t}\frac{\mathrm{A}}{k}\right| (\left|-\frac{1}{2t}\frac{1}{k}\right| \sigma_{\mathrm{A}} + \left|\frac{\mathrm{A}}{2t}\frac{1}{k^2}\right| \sigma_{\mathrm{k}}) \tag{A3}$$

$$\frac{\sigma_{\mathrm{D}}}{D} = \frac{\sigma_{\mathrm{A}}}{|A|} + \frac{\sigma_{\mathrm{k}}}{|k|} \tag{A4}$$

$$\sigma_{\mathrm{A}} = \begin{cases} \Delta X \left|\frac{X_{\mathrm{f}}-X_{\mathrm{a}}}{\Delta X}\right| (\sigma_{\mathrm{C}} + |-1|\sigma_{\mathrm{C}}) + |X_{\mathrm{f}}|(\sigma_{\mathrm{C}} + |-1|\sigma_{\mathrm{C}}), & X < 0 \\ \Delta X \left|\frac{X_{\mathrm{e}}-X_{\mathrm{f}}}{\Delta X}\right| (\sigma_{\mathrm{C}} + |-1|\sigma_{\mathrm{C}}) + |X_{\mathrm{f}}|(\sigma_{\mathrm{C}} + |-1|\sigma_{\mathrm{C}}), & X > 0 \end{cases} \tag{A5}$$

$$\sigma_{\mathrm{A}} = \begin{cases} -2X_{\mathrm{a}}\sigma_{\mathrm{C}}, & X < 0 \\ 2X_{\mathrm{f}}\sigma_{\mathrm{C}}, & X > 0 \end{cases} \tag{A6}$$

For interior points:

$$\sigma_{\mathrm{k}} = \frac{1}{12\Delta X}(\sigma_{\mathrm{C}} + |-8|\sigma_{\mathrm{C}} + 8\sigma_{\mathrm{C}} + |-1|\sigma_{\mathrm{C}}) = \frac{3}{2\Delta X}\sigma_{\mathrm{C}} \tag{A7}$$

For end-points:

$$\sigma_{\mathrm{k}} = \frac{1}{12\Delta X}(|-25| + 48\sigma_{\mathrm{C}} + |-36|\sigma_{\mathrm{C}} + 16\sigma_{\mathrm{C}} + |-3|\sigma_{\mathrm{C}}) = \frac{32}{3\Delta X}\sigma_{\mathrm{C}} \tag{A8}$$

$$\frac{\sigma_{\mathrm{D}}}{D} = \begin{cases} \dfrac{-2X_{\mathrm{a}}\sigma_{\mathrm{C}}}{|A|} + \dfrac{\frac{3}{2\Delta X}\sigma_{\mathrm{C}}}{|k|}, & X < 0, \text{interior points} \\ \dfrac{2X_{\mathrm{f}}\sigma_{\mathrm{C}}}{|A|} + \dfrac{\frac{3}{2\Delta X}\sigma_{\mathrm{C}}}{|k|}, & X > 0, \text{interior points} \\ \dfrac{-2X_{\mathrm{a}}\sigma_{\mathrm{C}}}{|A|} + \dfrac{\frac{32}{3\Delta X}\sigma_{\mathrm{C}}}{|k|}, & X < 0, \text{end} - \text{points} \\ \dfrac{2X_{\mathrm{f}}\sigma_{\mathrm{C}}}{|A|} + \dfrac{\frac{32}{3\Delta X}\sigma_{\mathrm{C}}}{|k|}, & X > 0, \text{end} - \text{points} \end{cases} \tag{A9}$$

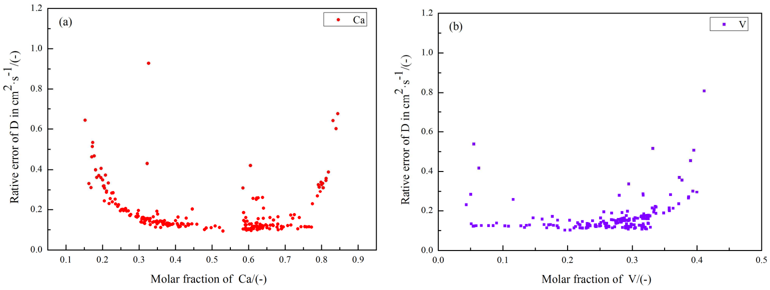

Fig. A1. Relative errors of the calculated Ca^{2+} interdiffusion coefficients and V^{5+} interdiffusion coefficients.